Shape Transitions and Lattice Structuring of Ceramide-Enriched Domains Generated by Sphingomyelinase in Lipid Monolayers

Steffen Härtel,*[†] María Laura Fanani,* and Bruno Maggio*

*Departamento de Química Biológica-CIQUIBIC, Facultad de Ciencias Químicas-CONICET, Universidad Nacional de Córdoba, Ciudad Universitaria, Córdoba, Argentina; and [†]Centro de Estudios Científicos, Valdivia, Chile

ABSTRACT   Sphingomyelinases (SMases) hydrolyze the membrane constituent sphingomyelin (SM) to phosphocholine and ceramide (Cer). Growing evidence supports that SMase-induced $SM \rightarrow Cer$ conversion leads to the formation of lateral Cer-enriched domains which drive structural reorganization in lipid membranes. We previously provided visual evidence in real-time for the formation of Cer-enriched domains in SM monolayers through the action of the neutral *Bacillus cereus* SMase. In this work, we disclose a succession of discrete morphologic transitions and lateral organization of Cer-enriched domains that underlay the SMase-generated surface topography. We further reveal how these structural parameters couple to the generation of two-dimensional electrostatic fields, based upon the specific orientation of the lipid dipole moments in the Cer-enriched domains. Advanced image processing routines in combination with time-resolved epifluorescence microscopy on Langmuir monolayers revealed: 1), spontaneous nucleation and circular growth of Cer-enriched domains after injection of SMase into the subphase of the SM monolayer; 2), domain-intrinsic discrete transitions from circular to periodically undulating shapes followed by a second transition toward increasingly branched morphologies; 3), lateral superstructure organization into predominantly hexagonal domain lattices; 4), formation of super-superstructures by the hexagonal lattices; and 5), rotationally and laterally coupled domain movement before domain border contact. All patterns proved to be specific for the SMase-driven system since they could not be observed with Cer-enriched domains generated by defined mixtures of SM/Cer in enzyme-free monolayers at the same surface pressure ($\Pi = 10$ mN/m). Following the theories of lateral shape transitions, dipolar electrostatic interactions of lipid domains, and direct determinations of the monolayer dipole potential, our data show that SMase induces a domain-specific packing and orientation of the molecular dipole moments perpendicular to the air/water interface. In consequence, protein-driven generation of specific out-of-equilibrium states, an accepted concept for maintenance of transmembrane lipid asymmetry, must also be considered on the lateral level. Lateral enzyme-specific out-of-equilibrium organization of lipid domains represents a new level of signal transduction from local (nm) to long-range (μm) scales. The cross-talk between lateral domain structures and dipolar electrostatic fields adds new perspectives to the mechanisms of SMase-mediated signal transduction in biological membranes.

INTRODUCTION

Phospholipases are a heterogeneous group of metabolic proteins that transduce lipid-specific signals at the membrane level (Wakelam et al., 1993; Exton, 1994; Krönke, 1999). Despite their structural and functional diversity, the activity of each lipolytic enzyme depends only on a few generic surface parameters. Lateral surface pressure, lipid composition and packing, phase coexistence, and surface electrostatics regulate enzymatic activities within narrow ranges (Jain and Berg, 1989; Honger et al., 1997; Muderhwa and Brockman, 1992; Maggio, 1966; Basañez et al., 1996). Due to the extreme sensitivity of their catalytic activity on subtle changes of the physicochemical conditions of the lipid interface, the precise molecular regulation of these enzymes can only be studied in systems with a rigorous control of the substrate organization

(Bianco et al., 1989, 1990; Maggio, 1999; Grainger et al., 1990; Ransac et al., 1991; Honger et al., 1997; Fanani and Maggio, 1997; Jungner et al., 1997; Liu and Chong, 1999).

Many studies have shown that the activity of lipolytic enzymes is favored by *membrane defects* that can be introduced by changes of lipid composition, anisotropically organized lipid substrates, phase coexistence, connectivity of the lipid phase domains (percoregulation), and tensions along the interfacial plane (Jain and Berg, 1989; Honger et al., 1997; Muderhwa and Brockman, 1992; Maggio, 1966; Basañez et al., 1996; Roberts, 1996; Heinz et al., 1998; Gatt, 1999). In this context, the regulation of the activity of PLA$_2$ (Liu and Chong, 1999) and cholesterol oxidase (Wang et al., 2004) has been related to several critical amounts of cholesterol that induce specific regular superlattice structures over ranges that exceed the local molecular interactions in lipid surfaces (Somerharju et al., 1985, 1999; Chong, 1994; Virtanen et al., 1988, 1995; Chong and Sugár, 2002). PLA$_2$ activity has also been reported to be altered by Cer-induced defects in phosphatidylcholine interfaces (Huang et al., 1999; Fanani and Maggio, 1997). For sphingomyelinase (SMase)-driven conversion of sphingomyelin (SM) to ceramide (Cer) we could show that SMase not only sculptured the surface topography but also that the variations of the latter affected the

time course of the reaction (Fanani et al., 2002). Since phospholipases generate second messengers that are involved in cascades of membrane-mediated signaling, the surface modulation of the activity of phospholipases represents a convergent point for biochemical and structural information exchange. In this context, local enzymatic alterations of chemical lipid structures are transduced to the intermolecular level through defined lipid interactions, leading to variations of membrane properties which, in turn, regulate activity and affect cross-communication between different phospholipase pathways (Fanani and Maggio, 1998). Lipid mixing-demixing processes and the concomitant structuring of segregated domains with different lipid composition or phase state profoundly influences precatalytic and catalytic steps of the phosphohydrolytic reactions (Bianco et al., 1991; Grainger et al., 1990; Fanani and Maggio, 2000; Fanani et al., 2002; Ruiz-Arguello et al., 2002).

Fundamental cellular processes like proliferation, differentiation, and cell death are triggered by the locally and temporally stimulated activation of different SMases that hydrolyze SM to phosphocholine and Cer (Levade and Jaffrézou, 1999; Hannun and Luberto, 2000; Szabo et al., 2004). Cer functions as a key pivotal compound that links the metabolism of phospho-, sphingo-, and glycosphingo-lipids, all of which can control phospholipase activity and membrane topology (Bianco et al., 1991; Basañez et al., 1996; Saéz-Cirión et al., 2000; Maggio, 1994; Maggio et al., 2004). Besides the conception of Cer as an important second messenger (Kolesnick et al., 2000), several authors have reported direct structural consequences of SMase-driven $SM \rightarrow Cer$ conversion in biological membranes. Primary structural consequences involve the formation of lateral Cer-enriched lipid domains (Holopainen et al., 1997, 2001) and the dilution of SM-enriched membrane rafts (Gulbins et al., 2004). Secondary structural consequences of lateral lipid reorganization concern physical membrane parameters like permeability (Ruiz-Arguello et al., 1996) as well as three-dimensional sculpturing of membrane vesicles (Holopainen et al., 2000), or the formation of apoptotic bodies (Tepper et al., 2000). Finally, structural reorganization has been reported to couple back to cellular signaling through the agglomeration of CD-95 and different ion channels in Cer-enriched membrane domains (Szabo et al., 2004; Gulbins et al., 2004).

Several studies have reported lateral phase segregation of Cer-enriched domains in model membrane systems (Holopainen et al., 1997, 1998; Huang et al., 1999; Carrer and Maggio, 1999; Carrer et al., 2003; Ruiz-Arguello et al., 2002). We provided the first direct visual evidence in real-time for SMase-induced formation of Cer-enriched domains in SM monolayers under precise control of the surface intermolecular packing (Fanani et al., 2002). The results revealed a bidirectional communication between effects taking place at the local catalytic level and the supramolecular surface organization. The present work employs improved time-

resolved epifluorescence microscopy of the SMase-driven reaction and of predefined enzyme-free mixtures of SM/Cer in combination with advanced image processing routines. We disclose a series of morphologic transitions, a defined hexagonal surface organization (super-structures), and the generation of long-range topographic pattern (super-super-structures) of the evolving SMase-generated Cer-enriched domains and apply theories of lateral shape transitions (McConnell, 1990; Vanderlick and Möhwald, 1990) and dipolar electrostatic interactions between lipid domains (McConnell, 1991, 1993; Nassoy et al., 1996) to reveal the underlying physical properties that lead to the SMase-driven regulation of surface architecture.

MATERIALS AND METHODS

Chemicals

Bovine brain sphingomyelin (SM) and ceramide (Cer) were purchased from Avanti Polar Lipids (Alabaster, AL). *Bacillus cereus* sphingomyelinase (SMase) was obtained from Sigma-Aldrich (Lot No. 48H4058, St. Louis, MO). The lipophilic fluorescent probe 1,1′-didodecyl-3,3,3′,3′-tetramethylindocarbocyanine perchlorate (DiIC$_{12}$) was purchased from Molecular Probes (Eugene, OR). NaCl was roasted at 500°C for 4 h.

Solvents and chemicals were of the highest commercial purity available. Surface-active impurities in the solvents and buffers were checked as described in Fanani and Maggio (1997).

Lipid monolayers and epifluorescence microscopy

All experiments were carried out at room temperature. Isotherms of surface pressure and surface (dipole) potential as a function of the mean molecular area of SM, Cer, and their defined mixtures at different molar concentrations were determined at 25°C (Fanani and Maggio, 1998; Fanani et al., 2002). The values of mean molecular areas, surface potential per unit of molecular surface density ($\Delta V/n$), and resultant dipole moment density perpendicular to the water surface (μ) were calculated directly from the compression isotherms (Maggio, 1999). SM/DiIC$_{12}$ and SM/Cer/DiIC$_{12}$ monolayers (0.5 mol % of DiIC$_{12}$) were obtained by spreading 20 μl of lipid solution in chloroform-methanol (2:1) over a subphase of 10 mM Tris-HCl, 125 mM NaCl, and 3 mM MgCl$_2$, pH 8, until reaching a surface pressure of ~0.5 mN/m (Fanani and Maggio, 1997). After solvent evaporation (10 min), the monolayer was compressed slowly to the desired surface pressure (Π = 10 mN/m) and equilibrated for 15 min. As previously reported, SM and Cer show low lateral miscibility (<12%) and form Cer-enriched domains (Fanani et al., 2002). Epifluorescence microscopy (Zeiss Axioplan, Carl Zeiss, Oberkochen, Germany) was carried out at 25°C with a mercury lamp (HBO 50), a 20× objective, a rhodamine filter set, and an all-Teflon zero-order trough (Kibron μ-Trough S; Kibron, Helsinki, Finland) mounted on the microscope stage. Monolayer flow was restricted with an open-end Teflon mask with a vertical slit covering the objective and extending through the film into the subphase. Images (exposure times 0.1–0.3 s) were registered with a software-controlled (Metamorph 3.0, Universal Imaging, Union City, CA), charge-coupled device (CCD) camera (Micromax, Princeton Instruments, Downingtown, PA).

Determination of enzymatic activity

As previously reported, the determination of enzymatic activity is based upon the different cross-sectional areas of SM (~84 Å^2) and Cer (~51 Å^2) in lipid monolayers at 10 mN/m (Fanani and Maggio, 1997; Fanani et al.,

2002). The enzymatic reaction was followed in real-time after injection of a diluted solution of SMase into the subphase of the reaction compartment (2 ml; 3.14 cm^2), reaching a final bulk concentration of 228 pmol/ml. The reaction compartment consists of a circular trough with an adjacent reservoir compartment whose surfaces are connected through a narrow and shallow slit. The time course of the SMase-driven $SM{\rightarrow}Cer$ conversion was determined by recording the reduction of the total monolayer surface area at a constant surface pressure of $\Pi = 10$ mN/m. The constant surface pressure was maintained automatically by the film barriers of the surface balance which replenished a film of pure SM from the reservoir compartment (Fanani and Maggio, 1998). A detailed analysis of the two-dimensional kinetics was previously published and the rate constants of the different steps of the reaction were identified and determined (Fanani and Maggio, 2000). It was shown that the reaction lag time was due to a slow bimolecular surface activation of the enzyme, followed by a pseudo zero-order kinetic regime in which the reaction proceeded with a constant rate at a constant enzyme concentration (irreversibly adsorbed to the interface; see Fanani and Maggio, 2000). During this period the reaction rate is independent of the surface concentration of SM. The substrate is in excess with respect to the enzyme

until the accumulation of the Cer causes a slowdown of the rate and progressive halting of the reaction (see Fig. 1 a, $inset$). We also performed experiments of film-transfer to enzyme-free subphases which showed that the steady-state, pseudo zero-order rate was unaltered. This demonstrated that the reaction was truly two-dimensional and carried out by the tiny catalytic amounts of enzyme, adsorbed irreversibly to the interface. In addition, experiments with iodinated radioactive enzyme indicated that the formation of Cer did not cause enzyme desorption that could lead to the slowing down of the reaction after the steady-state period. The determination of the amount of adsorbed enzyme yielded a substrate/enzyme ratio between 1.2 and 2.4 10^4, which represents an excess substrate of $\sim$2000 times the value of the two-dimensional K_M (Fanani and Maggio, 2000). Additionally, the variation of the amount of adsorbed enzyme changes the metabolic rate proportionally, as long as the surface concentration of SM remains at least 10 times above K_M. Although the substrate is continuously replenished from the adjacent reservoir to the reaction compartment (Fanani and Maggio, 1998), Cer-enriched domains accumulate until $\sim$80% of the original surface concentration of SM in the reaction compartment is metabolized and the reaction halts (Fig. 1, this article; see also Fanani et al., 2002). This observation also supports the
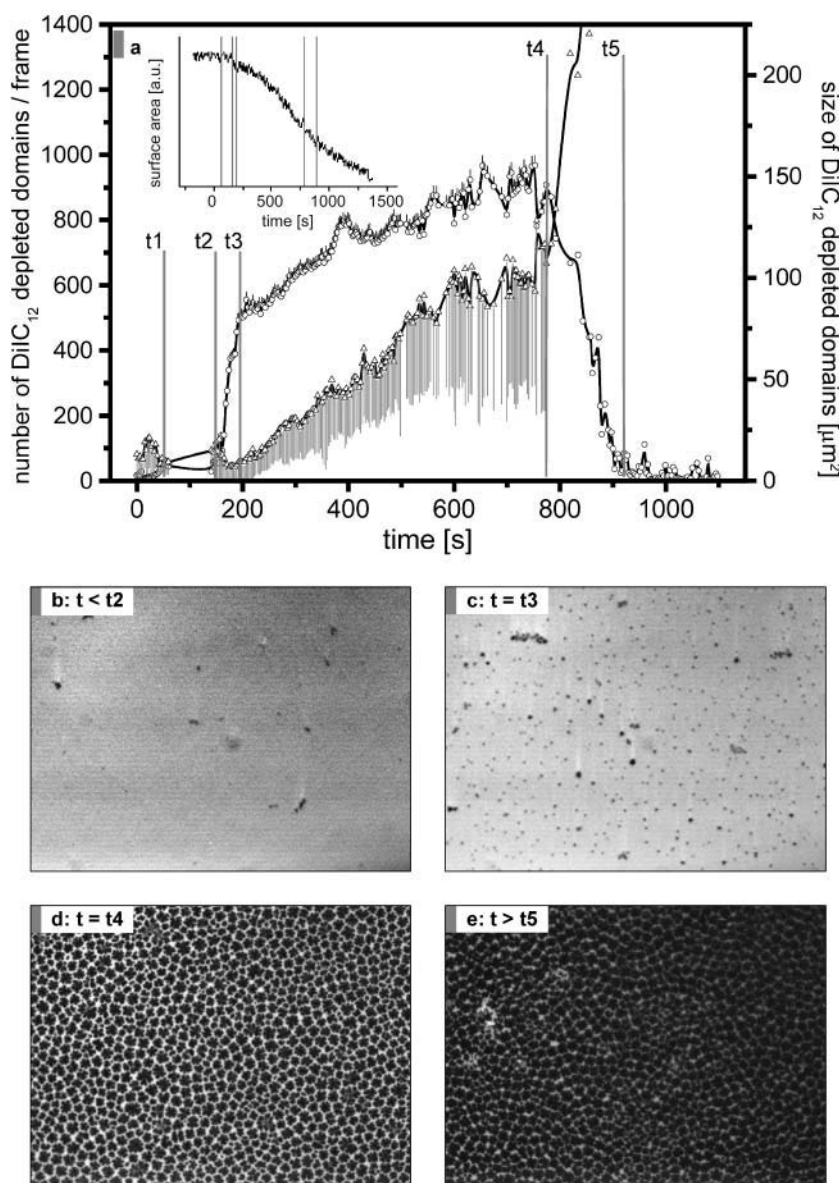

FIGURE 1 Time course of SMase-driven $SM{\rightarrow}Cer$ conversion and simultaneous formation of Cer-enriched lipid domains at a constant surface pressure ($\Pi = 10$ mN/m). Dark-shaded regions in b–e represent the formation of Cer-enriched lipid phases with unfavorable partition conditions for the lipophilic fluorescent dye DiIC$_{12}$. (a) Number ($open$ $circles$) and mean size ($open$ $triangles$) of DiIC$_{12}$-depleted domains as derived by segmentation of Cer-enriched lipid domains from the digital picture series (x,y-dimension $= 450 \times 354$ μm). Symbols are connected by β-splines. Number and mean area of DiIC$_{12}$-depleted domains were calculated by image-processed epifluorescence microscopy (see Materials and Methods). Error bars were calculated until t4 (beginning of domain border contact) and defined the SD for the corresponding populations ($\sqrt{N}$ for counting experiments). ($Inset$) Time-dependent reduction of the total film area by the surface barrier movement of the barostat at constant surface pressure ($\Pi = 10$ mN/m). (b–e) Representative microscopic CCD images (x,y-dimension 450×354 μm) of DiIC$_{12}$ fluorescence in SM monolayers (high dye concentration/bright fluorescence) and in Cer-enriched domains (low dye concentration/fluorescence). The images visualize discrete stages at selected times t of the enzymatic reaction (b, $t \leq t$2; c, $t = t$3; d, $t = t$4; and e, $t \geq t$5. Compare to shaded vertical lines in a).

interpretation of the film-transfer experiment: SMase adsorbs irreversibly to the SM interface and increasing proportions of Cer do not impair the interfacial enzyme adsorption (Fanani and Maggio, 2000). Due to the accumulation of Cer-enriched domains, the rate eventually decreases and the reaction cannot be defined as a true zero-order kinetics, as in other hydrolytic reactions where soluble products desorb immediately from the interface (e.g., PLA$_2$ or PLC; Bianco et al., 1989, 1990); in these cases an indefinitely constant rate under true zero-order conditions is achieved as long as the substrate is replenished continuously from the adjacent monolayer reservoir. To point out this important difference, we denominate the SMase-catalyzed reaction as pseudo zero-order during the linear period of the catalysis.

Computational analysis of surface properties

The lipophilic fluorescent probe DiIC$_{12}$ shows preferential partition in the LE phase of the lipid monolayer (Spink et al., 1990). LE and LC lipid phases are represented by bright (high fluorescence/DiIC$_{12}$ enriched) and dark (low fluorescence/DiIC$_{12}$-depleted) pixels in the 8-bit image intensity interval ($I \in [0,255]$). In the recorded picture series (x,y-dimensions: 450×354 μm/ 658×517 pixels), segmentation of DiIC$_{12}$-depleted areas was achieved by interactive image processing routines written in IDL (Interactive Data Language, Research Systems, Boulder, CO) as described before (Fanani et al., 2002). The quality of the segmentation was optimized interactively by overlaying the calculated object masks with the original fluorescent pictures (see Supplementary Material, *SMaseMask.avi*). From the binary image masks of the segmented domains, parameters for the quantitative description of domain morphologies and lateral domain organization were extracted with the corresponding image processing routines listed below. Morphologic features were calculated for Cer-enriched lipid domains, formed by the SMase-driven system (Figs. 1–4, 6, and 7) and by the predefined lipid mixtures of SM/Cer (Figs. 4–7). Lateral domain lattice organization was calculated for both experimental systems (Fig. 4), and for virtual Cer-enriched domain centers which were seeded randomly onto a SM monolayer surface (450×354 μm/658×517 pixels) by a small computer routine (see below and Fig. 3).

The following morphologic domain features were calculated:

The number of unconnected Cer-enriched domains per image frame; the connectivity of object domains in the binary object masks was defined with a four-neighbor algorithm. After that, unconnected objects were numbered and counted automatically in the corresponding image frames.

The area (A) of the lipid domains was calculated from the number of pixels in the segmented binary object masks and the known pixel size (0.684×0.685 μm^2).

The object border trajectories enclosing the Cer-enriched lipid domains were parameterized by the Freeman chain code (Freeman, 1970). The calculation of the length of the border trajectories or perimeter P was accomplished as described before (Härtel et al., 2003).

The curvature of the object trajectories and the number of saddle points was also derived from the presentation of the object border trajectories in the Freeman chain code.

The zoom-invariant shape-sensitive parameter circularity (P^2/A) was determined by the division of the square of the perimeter of a domain by its respective area.

The following parameters characterize the lateral domain organization:

For the calculation of the domain centers of the irregularly shaped Cer-enriched lipid domains, we used the calculation of the translation-, rotation-, and zoom-invariant moments according to Castleman (1996). In the course of their calculation, the centers of gravity [x',y'] are derived from the first- and zero-order order moments: $x' = M_{10}/M_{00}$ and $y' = M_{01}/M_{00}$.

For every segmented domain, two parameters were calculated to characterize the nearest domain distance. First, the minimum border distance

(r_b) calculates the minimal distance from the border of each domain to the border of the closed domain neighbor. The minimum center distance (r_c) does the same with respect to the domain centers. Note that the nearest-neighbor with respect to the border distances is not necessarily the same nearest-neighbor with respect to the center distance.

The parameter highest-gap distance (hgd) is calculated as follows: 1), for each segmented Cer-enriched domain in an image frame, the domain centers are calculated as described above; 2), for each center, the Euclidean distances to the 10 most proximate domain centers are determined; and 3), distances are sorted by size into a vector, and the ranking position (1–10) of the distance with the highest gap to the following distance is defined as the hgd (for an hexagonal lattice structure the hgd-value will be 6; for a pentagonal lattice structure the hgd-value will be 5; etc.).

Calculation of the electrostatic field and the interdomain energy of Cer-enriched domains:

The electrostatic field E generated at a distance r_d from a unit domain area (one pixel: $\Delta x \Delta y = 0.684 \times 0.685$ μm^2) was calculated by $E(r_d) = \mu/(4\pi \times \varepsilon_0 \times \varepsilon) \times (1/r_d^3) \times \Delta x \Delta y$. In this equation, μ is the difference of the dipole moment densities of the lipid domains composed of pure Cer or SM ($\mu = \mu_{Cer} - \mu_{SM}$, see Fig. 6), $\varepsilon_0 = 8.85$ 10^{-12} [CV^{-1} m^{-1}] is the dielectric constant in vacuum, and ε is the effective dielectric constant at the air/water interface (for the calculation of electric fields of lipid domains, $\varepsilon \sim 7$ yielded good agreement with experimental results based on solvatochromic measurements in sphingolipid interfaces (Montich et al., 1985) and from the determination of the velocities of electrically charged microspheres (Nassoy et al. 1996). Following the latter authors, the energy $W(r_d)$ acquired by a dipolar probe is given by the scalar product between the dipole μ' and $E(r_d)$. For one unit lipid domain area, μ' is calculated by $\mu' = \mu \cdot \Delta x \Delta y$, and the energy between two unit domain areas results in $W(r_d) = \mu^2/(4\pi \times \varepsilon_0 \times \varepsilon) \times (1/r_d^3) \times \Delta x \Delta y^2$. The sum over all pixel combinations of two domains A and B, $W(AB) = \Sigma_A \Sigma_B W(r_{AB}) = (\mu^2 \times \Delta x \Delta y^2/(4\pi \times \varepsilon_0 \times \varepsilon)) \times \Sigma_A \Sigma_B (1/r_{AB}^3)$ (Eq. 1), finally yields the total interdomain energy between the respective domains. This procedure can be expanded successively to calculate the interdomain energies between a higher numbers of domains.

RESULTS AND DISCUSSION

As reported previously (Fanani and Maggio, 1998), the SMase-driven $SM \rightarrow Cer$ conversion in SM monolayers was determined by following the reduction of the surface area on the reaction compartment at a constant surface pressure $\Pi = 10$ mN/m (Fig. 1 *a*, *inset*). The molecular kinetics underlying the different precatalytic and catalytic steps responsible for the shape of the reaction curve has been discussed in detail before (Fanani and Maggio, 2000):

1. SMase is injected into the subphase of the SM monolayer (*first vertical shaded line* in the *inset* of Fig. 1).
2. SMase partitions rapidly to the substrate film through a diffusion-limited process.
3. A lag-time period is due to a slow, precatalytic, bimolecular enzyme activation step at the interface.
4. SMase-driven $SM \rightarrow Cer$ conversion reaches a transient steady-state rate (pseudo zero-order kinetics).
5. The $SM \rightarrow Cer$ conversion is halted due to the surface enrichment in Cer which limits substrate availability (Fanani and Maggio, 2000; Fanani et al., 2002).

The continuous and progressive reduction of the total film area (Fig. 1 *a*, *inset*) suggests a smooth change of molecular composition at the surface during the evolution of the SMase-driven $SM \rightarrow Cer$ conversion. However, the time-resolved computational analysis of the monolayer surface topography reveals a succession of discrete stages which are concomitant to defined catalytic steps of the reaction and will be described in detail below.

SMase-generated Cer-enriched domains undergo morphologic transitions

In Fig. 1 *a*, the SMase-driven formation of Cer-enriched domains in SM monolayers is characterized by the number and the mean area of the segmented $DiIC_{12}$-depleted areas in the digital picture series taken during the catalytic reaction (Fig. 1, *b–e*). The first shaded vertical line (*t*1 in Fig. 1 *a*) marks the injection of SMase into the subphase of the reaction compartment and *t*2 (Fig. 1, *a* and *b*) marks the beginning of detectable $SM \rightarrow Cer$ conversion by the reduction of the total film area. During a time period of ~40 s (*t*2–*t*3), Cer-enriched domains form spontaneously at an approximately linear rate (~12 s^{-1}). At *t*3 (Fig. 1, *a* and *c*), the rate of spontaneous domain formation abruptly decreases and the areas of Cer-enriched domains start to grow linearly until the domain borders cannot be separated any longer on the chosen

microscopic scale (*t* > *t*4). That period correlates with the catalytic reaction entering, and remaining, in the pseudo zero-order steady state of the $SM \rightarrow Cer$ conversion (Fig. 1, *a* and *d*). At *t* > *t*5, Cer-enriched domains finally form a single connected phase whereas $SM \rightarrow Cer$ conversion persists at a slow rate until ~80% of the total SM has been converted to Cer. At this point, only traces of the LE phase of the SM monolayer remain encapsulated between the Cer-enriched domains (Fig. 1, *a* and *e*).

During the linear growth of the mean areas of the Cer-enriched domains simultaneous to the steady-state reaction (*t*3–*t*4), several morphologic parameters reveal successive shape transitions which mark discrete shape instabilities of the two-dimensional domains (Fig. 2). Right after the spontaneous domain formation (*t*3) the mean number of saddle points of the domain border trajectories remains constant, until the parameter starts to grow steadily at *t* > *t*3′. In 1990, Vanderlick and Möhwald introduced the discrete mode ($m \in [0, 1, 2, \ldots]$) and the relative amplitude of undulation ($\varepsilon \in [0–1]$) for the description of shape transitions from circular to regularly undulated lipid domains. With *m* and *ε*, the domain shape can be parameterized by the border trajectory $R(\Theta) = \Lambda(1 + \varepsilon \cdot \cos(m \cdot \Theta))$ (Eq. 2), using polar coordinates ($\Theta \in [0, 2\pi]$) and the mean radius of the lipid domain Λ. It should be emphasized that the number of saddle points of a border trajectory of a closed lipid domain (*n*) can only adopt even
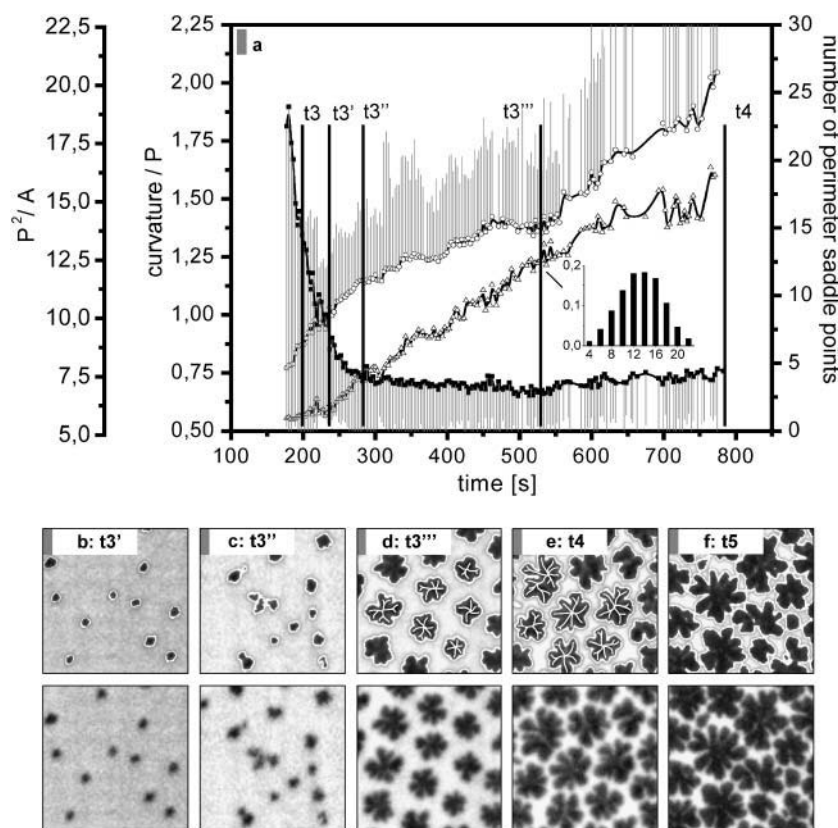

FIGURE 2 Shape transitions of Cer-enriched domains during the time course of SMase-driven $SM \rightarrow Cer$ conversion. (*a*) Mean values of the morphologic parameters: P^2/A (*open circles*), the curvature of the border trajectory normalized by the length of border trajectory (i.e., curvature/perimeter; *solid squares*), and the number of saddle points of the border trajectories (*open triangles*) are connected by *β*-spline curves. All parameters were derived by image-processed epifluorescence microscopy, as described in Materials and Methods. At *t*3, the rate of spontaneous domain formation falls abruptly and Cer-enriched domains start to grow in a linear manner until the percolation of the domains at *t* = *t*4 (compare to Fig. 1). Error bars define SD for P^2/A and the normalized curvature. For the population intrinsic variation of the number of saddle points of the border trajectories, we show a representative normalized frequency distribution of a total of 725 Cer-enriched domains at *t* = *t*3‴ (*d*). (*b–f*) Representative microscopic picture series (51.3 × 51.3 μm) of $DiIC_{12}$-depleted Cer-enriched domains in SM monolayers visualize morphologically discrete stages at different times of the enzymatic reaction. (*b*, *t*3′; *c*, *t*3″; *d*, *t*3‴; *e*, *t*4; and *f*, *t*5 correspond to vertical shaded lines in *a*, this figure, and in Fig. 1 *a*. Domain borders in the upper row are highlighted by open edges. As the morphologic parameters in *a* suggest, the Cer-enriched domains start to grow in a circular manner, until successive branching is detected. To outline the transition from first-order to second-order branching, branches were sketched manually into the domains in *d* and *e* (*upper row*).

numbers $n \in [0, 2, 4, \ldots]$ which are directly correlated to m by a factor of 2 ($n = 2 \cdot m$). In Fig. 2, we derived n from all domain border trajectories segmented in the CCD-images without prior mode selection. In this manner, defects or impurities in the lipid phase which possess high numbers of border trajectory perturbations (see Fig. 1, *b* and *c*, and Fig. 2 *c*) are included in the plotted mean values. A closer look at the population statistics reveals that ~85% of all segmented domains correspond to the group of freshly nucleated Cer-enriched domains that do not present any border trajectory undulations during the initial part of the SMase-driven Cer formation ($t < t3'$, data not shown). Right after the spontaneous formation of Cer-enriched domains ($t3$), the circular population is characterized by a mean domain area (A) of $A(t3) = 6 \pm 3.2$ (standard deviation, i.e., SD) μm^2. The domain areas continue to grow in a circular manner until first-domain border undulations can be detected at $t3'$. At this time, the domains have almost doubled their area to $A(t3') = 11 \pm 4.5$ μm^2 (Fig. 2, *b* and *c*). At $t > t3'$ the number of perimeter saddle points (n) grows steadily into an average number of ~18 (corresponding to $m = 9$ border undulations), before the domain borders start to touch at $t4$ (Fig. 2, *d–f*). At this time, the kinetics enters the end of the pseudo zero-order steady-state catalysis and the reaction rate falls (Fig. 1, *inset*).

Based on the theoretical treatment of harmonic shape transitions from circular domains to shapes with a higher rotation symmetry (McConnell, 1990) or on computer simulations (Vanderlick and Möhwald, 1990), the critical radius r_m at which a circular domain becomes unstable with respect to a shape with a m-fold rotation symmetry (or border undulation) is given by $r_m = d \cdot e^{Z_m} \cdot e^{\lambda}/\mu^2/4$ (Eq. 3). In this equation, λ is the line tension at the domain boundary, μ is the difference in the dipole moment density between the segregated lipid domains and its surrounding lipid phase, d is the molecular distance between neighboring dipoles, and Z_m are shape transition exponents defined by the geometrical rotation symmetry m. We can determine r_m directly from the critical area of the domains at the point of the shape transition ($t3'$): $r_m(t3') = (A(t3')/\pi)^{0.5} = 1.87 \pm 0.35$ μm. The frequency of the modes m for the Cer enriched domains after the first shape transition ($t3'$) can be derived directly from the number of saddle points: $m = n/2$. The inset of Fig. 2 *a* shows a normalized histogram for a total of 725 Cer-enriched domains at $t3'''$ whose frequency values follow a Gaussian-like distribution which centers between $n = 12$ and 14, corresponding to $m = 6$ and 7, respectively. Using $Z_{m=6} = 12.88/3$ according to Vanderlick and Möhwald (1990) and calculating $d = 9.2$ Å from the mean distance between adjacent Cer molecules ($d_{Cer} = 2 \cdot r_{Cer} = 2 \cdot (51$ Å$^2/\pi)^{0.5} = 8.1$ Å) and SM molecules ($d_{SM} = 2 \cdot r_{SM} = 2 \cdot (84$ Å$^2/\pi)^{0.5} = 10.3$ Å), we derive the dimensionless number $\Gamma_{SMase, t3'} = \mu^2/\lambda = 1/\ln[4 \cdot r_m/(d \cdot e^{4.29})] = 0.212 \pm 0.008$. The value Γ relates the energy of the repulsive electrostatic interactions (μ^2) to the energy of the border-minimizing line tension (λ), which are the determinant factors for equilibrium shapes of two-dimensional lipid domains. With Γ_{SMase} and $Z_{m=0} = 3$ for circular lipid domains in equilibrium, Eq. 3 opens a direct access to the theoretical equilibrium size (A_{eq}): $A_{eq} = \pi \cdot (d \cdot e^3 \cdot e^{1/\Gamma}/4)^2 = 8.84 \pm 2.24$ μm^2. In conclusion, SMase-generated, Cer-enriched domains are characterized by an equilibrium size $A_{eq} \approx 8.8$ μm^2 which lies just between the size after the spontaneous domain formation $A(t3) \approx 6$ μm^2 and the critical domain size for the first shape transition $A(t3') \approx 11$ μm^2.

Further morphologic information is provided by the time course of the mean curvature of the border trajectories which are normalized by the perimeter (P) (Fig. 2 *a*). Right after the spontaneous domain formation ($t3$), the P-normalized curvature drops rapidly and passes over to its final constant level at $t3''$. A close observation of the domain morphology in the picture series (Fig. 2, *d–f*) reveals that the Cer-enriched domains maintain the P-normalized curvature through a combination of effects:

1. Cer-enriched domains perform consecutive shape transitions to higher modes m.
2. The relative amplitude of mode undulation ε increases successively from ~0.25 at $t3'$ to ~0.5 at $t4$ (estimated values for the domain shapes).
3. The apexes of existing modes m undergo successive branching or bifurcation.

Although higher modes m (*1*, above) and increasing ε (*2*, above) present variations inside of a defined class of shapes which can be parameterized by Eq. 2 (see Supplementary Material), the transition from first-order to secondary-order branching (*3*, above) cannot. The formation of substantially different shapes is clearly indicated by the area invariant descriptor of circularity (P^2/A) at $t3''$. The transition of first-order to second-order branching can also be observed in Fig. 2, *d* and *e*: the Cer-enriched domains adopt fractal-like shapes before their borders start to touch at $t > t4$. From $m = 9$ at $t4$, we can derive that an average of at least three out of six first-order branches provide secondary bifurcations (Fig. 2, *d* and *e*, *upper row*). A calculation of the fractal dimension of these domains yields values between 1.63 and 1.76, depending on the method applied for the calculation of fractality (box dimension, perimeter/area, or information dimension; Benoit 1.2, TrueSoft, McCabe Associates, Warwick, RI). This clearly indicates that these domain morphologies correspond to a self-similar structure.

The evolution of the morphology of Cer-enriched domains by SMase activity can also be characterized in terms of thermodynamic first- and second-order phase transitions (McConnell, 1991). Apart from the spontaneous domain nucleation that fulfills the criteria for a first-order phase transition, the conversion from circular shapes to shapes of higher harmonics as well as the fractal-like branching belong in the category of continuous second-order phase transitions; these shapes are topologically equivalent since they do not include discontinuities during the transitions (Peitgen et al.,

1998). Since the shape transition at $t3'''$ occurs approximately in the middle of the pseudo zero-order kinetic regime (see Fig. 7), the domain shape and their two-dimensional organization (see below) appear to represent an optimal structural code, signaling the maintenance of efficient steady-state catalysis. On the other hand, the appearance of secondary-order branching between $t3'''$ and $t4$ precedes the deviation of the reaction from pseudo zero-order kinetics, signaling a marked decrease of the reaction rate, and the gradual halting of $SM \rightarrow Cer$ conversion (Fig. 7).

SMase-generated Cer-enriched domains adopt hexagonal lattice formations

Complementing information about discrete stages in the organization of Cer-enriched lipid domains is provided by the nearest domain distances (Fig. 3 a). This parameter was calculated either with respect to the domain centers (r_c) (*solid circles*) or the domain borders (r_b) (*open circles* with the corresponding SDs). During the spontaneous formation of Cer-enriched domains ($t < t3$), both distances drop rapidly to $\sim$10 μm. After that, the nearest border distance drops at a rate of $\sim$0.012 μm/s to $\sim$7 μm whereas the nearest center distance increases up to a maximum value of $\sim$13 μm at $t3^X$. During this interval, the SD of the nearest border distance diminishes by a factor of 4. The increasing center distance and the diminishing SD of the border distances indicate specific interdomain interactions that organize the Cer-enriched domains directly after their spontaneous formation ($t3$). Without specific interactions, lipid domains are primarily subjected to random Brownian motion, which should not affect the average distribution of the domain distances (McConnell, 1991, 1993). Although the decreasing r_b could be explained by the growth of the domains, the reduction of the corresponding SD and the increase of r_c cannot. Lipid domain interactions are primarily governed by dipolar repulsion which exerts an ordering effect on the domain topology as soon as the repulsion energy competes with the thermal energy of magnitude k_bT (this point will be discussed in combination with Fig. 6 below). After $t3^X$, the
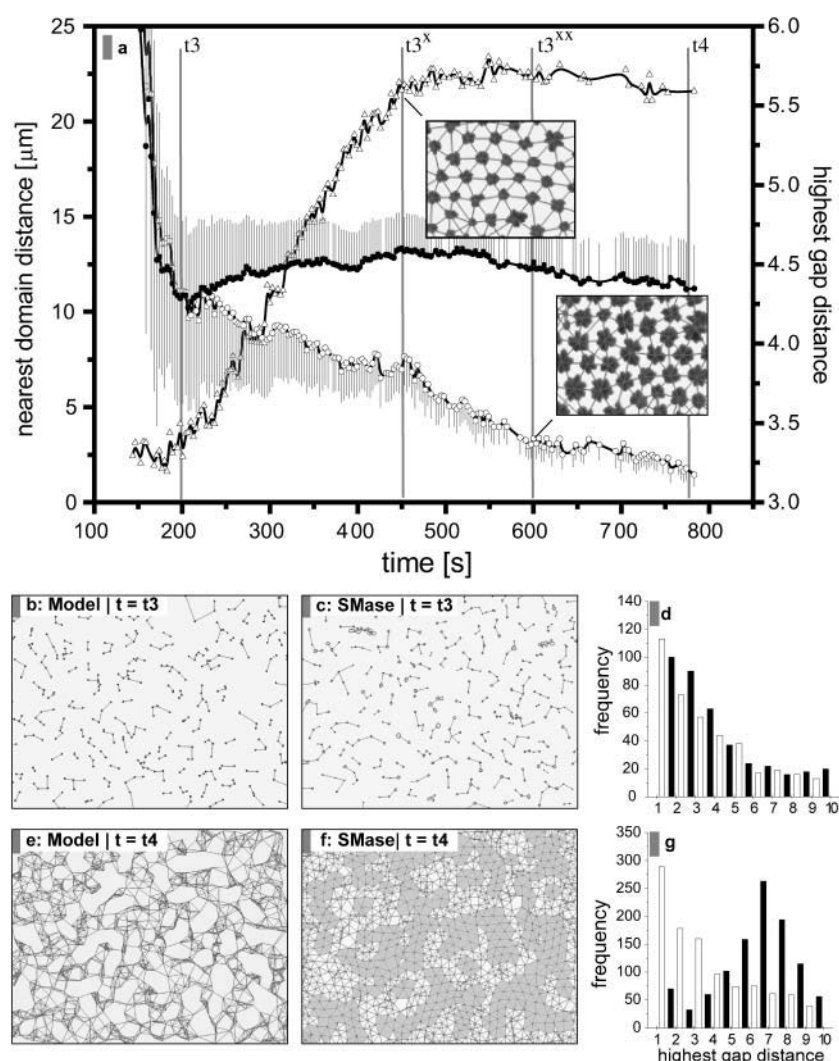

FIGURE 3 Formation of hexagonal Cer-enriched domain lattices as observed during the time course of SMase-driven $SM \rightarrow Cer$ conversion. (a) Lattice formation of Cer-enriched domains is monitored by different parameters. The mean values and the corresponding SD of the nearest domain distances between Cer-enriched domains are plotted for the center and border distances (*solid* and *open circles*, respectively). The mean values of the parameter of highest gap distance (hgd) are plotted as open triangles. The population intrinsic variation of this parameter can be estimated from d and g and c and f, (also see i, l, o in Fig. 4). Data points are connected by β-spline curves. The figure insets (x,y-dimension = 94 × 72 μm) visualize the hexagonal lipid domain distribution at $t3^X$ and $t3^{XX}$. (b–g) The parameter hgd is compared for randomly seeded domain centers (b and e) with the experimental situation established by SMase-driven $SM \rightarrow Cer$ conversion (c and f) at the beginning of the spontaneous domain formation ($t3$) (b and c) and before the percolation of the Cer-enriched domains ($t4$) (e and f). In the model systems (b and e), the number of the seeded domain centers reflects the conditions of the corresponding SMase-driven experiments (c and f). The areas b, c, e, and f represent x,y-dimensions of 450 × 354 μm. The histograms (d and g) plot the hgd-frequency distribution for randomly seeded domain centers (*open columns*) and the enzymatically generated domain centers (*solid columns*). The domain centers are connected with the first (b and c) and the first six nearest domain centers (e and f), reflecting the preferential-lattices formation in the SMase-driven system (c and f). In f, the hexagonal lattices are light-shaded to indicate the non-uniform distribution into a superlattice.

decrease of the nearest border distance accelerates to a rate of ~0.026 μm/s, reducing the nearest border distance to ~3 μm at $t3^{XX}$. During this time interval, the nearest center distance drops only slightly down to ~12 μm. At $t > t3^{XX}$, the decrease of the nearest border distance slows down to ~0.008 μm/s until the apparent percolation of the domains at $t4$. At this time, the nearest center distance has only been reduced to ~11 μm.

The visual perception of the organization of Cer-enriched domains during the SMase-driven $SM{\rightarrow}Cer$ conversion suggests the formation of a primarily hexagonal domain lattice (Figs. 1–3) which is also referred to as *supercrystal* or *superstructure* phases (McConnell, 1991). A perfect lattice formation with well-defined angular alignments cannot be expected in our experimental system, since size and shapes of the generated Cer-enriched domains are subjected to variations within their population. With the purpose of quantifying somewhat irregular domain lattices, we introduce the parameter of highest-gap distance (hgd) which indicates the type of lattice by reporting the frequencies of the number of closest nearest-neighbors to a domain in the lattice. To validate that hgd is an adequate descriptor for our system, we compared the frequency distributions of the hgd in stochastically originated model systems (Fig. 3, *b* and *e*) to hgd-frequency distributions derived from the SMase-driven experiment at two different stages of the enzymatic reaction (Fig. 3, *c* and *f*). The hgd-frequency distribution confirms that the domain centers are randomly distributed at the end of the spontaneous domain formation (*t3*, Fig. 3, *a–d*). At *t4* instead, the value with the highest hgd-frequency proves that the SMase-driven system predominantly forms a hexagonal lattice (Fig. 3, *f* and *g*). Apart from this important quantitative conclusion, the direct visualization of the connected domain centers highlights similarities between the random system and the SMase-driven experiment at *t3* (Fig. 3, *b* and *c*). Here, each domain center is connected to its nearest-neighbor, in accordance to the highest hgd-frequency (Fig. 3 *d*). At t4 instead (Fig. 3, *e* and *f*), each domain center is connected to its six nearest-neighbors, according to the highest hgd-frequency (Fig. 3 *g*). At this stage of the reaction (end of the pseudo zero-order, steady-state kinetics), a clear difference can be observed between the random model system and the SMase-driven experiment (Fig. 3, *e* and *f*).

The time course of the hgd-values during the SMase-driven SM→Cer-conversion depicts a surprisingly rapid organization of Cer-enriched domains from random distribution to a predominantly hexagonal domain lattice. Right after the spontaneous domain formation (*t3*), the mean values of the hgd (Fig. 3 *a*), the histogram (Fig. 3 *d*), and the CCD-image (Fig. 3 *c*) congruently support a random distribution of the Cer-enriched domains. At $t > t3$, the mean values of the hgd rise steeply, confirming that dipolar repulsion instantly exerts an ordering effect on the domain organization (see discussion of Fig. 6). During this period, the number of saddle points (border undulations) increase steadily, in-

dicating the predominance of repulsive dipolar energy over the border line-tension. At $t3^{X}$, the Cer-enriched domains have already adopted a predominantly hexagonal lattice formation. At this time, the transition between first- and second-order branching takes place (Fig. 2, *a–d*, and Fig. 7) and the enzymatic reaction enters the pseudo zero-order regime (Fig. 1 *a*, *inset*, and Fig.7). The predominantly hexagonal lattice formation is maintained until first domain borders start to touch at $t > t4$ (Fig. 3 *f*). Non-uniform clustering of the more regular hexagonal lattice units formed by the domain centers is clearly noticeable in Fig. 3 *f*, indicating an even higher level of superlattice structuring. The latter also shows a self-similar organization in the long-range with a fractal dimension of 1.83–1.86. In contrast, the random distribution with the same number of domain centers does not form self-similar structures (Fig. 3 *e*) and has a fractal dimension between 1.97 and 1.99 indicating no self-similarity (indistinguishable from the Euclidean dimension of 2 for a nonfractal surface).

Cer-enriched lipid domains generated by SMase activity or mixtures of SM/Cer adopt different morphologic properties and lattice organization

As we have shown in a previous publication (Fanani et al., 2002), mixtures of SM/Cer form a high number of Cer-enriched domains which cover a higher percentage of the total lipid monolayer area than the SMase-driven system at equal Cer concentrations. Finally, percolation of the domains occurs at lower Cer concentrations in the enzyme-free SM/Cer-mixtures. Figs. 4 and 5 reveal substantial differences in the lateral organization and in the morphology of Cer-enriched domains. The lattice organization of Cer-enriched domains generated by SMase activity is compared to domains generated by defined mixtures of SM/Cer at concentrations of 2, 5, 20, 30, and 50 mol % Cer in Fig. 4. At Cer-concentrations of 2 mol %, the hgd-frequency distribution indicates randomly distributed lipid domains in both systems (compare Fig. 4 *c* to Fig. 3, *b–d*). At Cer-concentrations of 5 mol %, the hgd-frequency distribution shifts to the right, indicating first repulsive interactions between the domains in both experimental systems (Fig. 4, *d–f*). At Cer-concentrations of 20 mol % (Fig. 4, *g* and *h*), the hgd-frequency distribution has strongly shifted to the right (Fig. 4 *i*). For the SMase-driven system, the distribution provides a sharp maximum at an hgd of six neighbors. The domains formed by the mixtures of SM/Cer also differ from randomly distributed lipid domains, but 1), the frequency distribution is significantly broader in comparison to the SMase-driven system; and 2), the most frequently formed lattice structure includes five, instead of six, nearest-neighbors. At Cer-concentrations of 30 mol %, the hgd-frequency distribution does not indicate any further increase in the order of the SMase-driven system (Fig. 4 *f*). For the domains formed by the SM/Cer-mixture
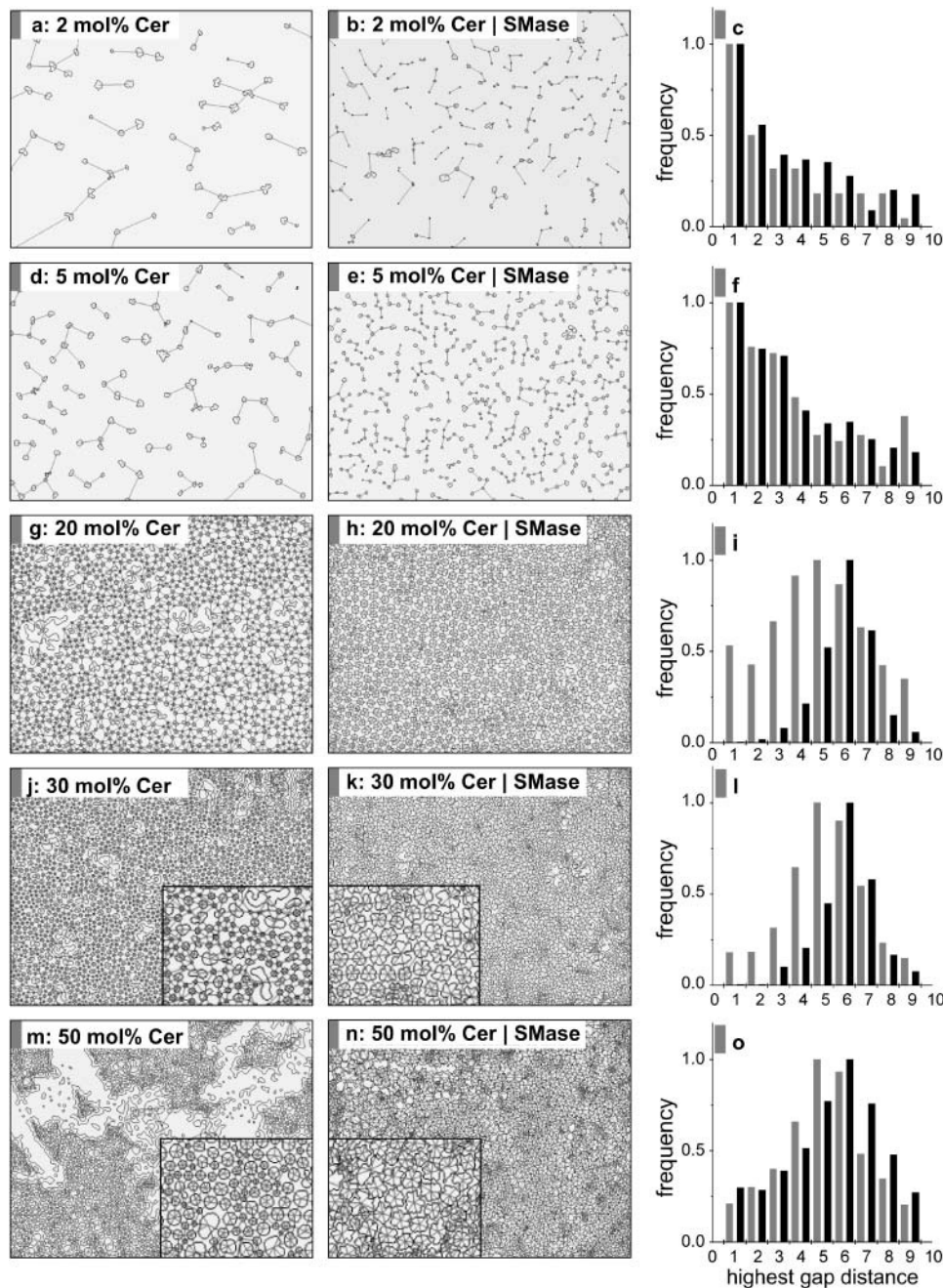
FIGURE 4 Comparative formation of Cer-enriched domain lattices as observed in defined mixtures of SM/Cer (*left column*) and during the time course of SMase-driven $SM \rightarrow Cer$ conversion (*center column*). The surface pressure in both systems is $\Pi = 10$ mN/m. Picture frames in the left and the center columns present *x,y*-dimensions of $450 \times 354 \ \mu m$. Amplified insets in *j*, *k*, *m*, and *n* have *x,y*-dimensions of $112.5 \times 88.5 \ \mu m$. The histograms (*right column*) present the parameter of highest gap distance for the defined mixtures of SM/Cer (*shaded columns*) and for the SMase-driven $SM \rightarrow Cer$ conversion (*solid columns*). The fraction of Cer increases from 2 mol % (*a–c*); 5 mol % (*d–f*); 20 mol % (*g–i*); 30 mol % (*j–l*); to 50 mol % (*m–o*).

instead, the order increases slightly, but the most frequent lattice structure still includes only five instead of six nearest-neighbors and has a broader distribution. At Cer-concentrations of 50 mol %, the hgd-frequency distributions shift slightly to the left for both experimental systems which is probably due to advanced percolation of the Cer-enriched domains (Fig. 4 *m*), and due to first touching domain borders (Fig. 4 *n*). In summary, Cer-enriched domains generated by mixtures of SM/Cer do not spontaneously form hexagonal domain lattices. Instead, hexagonal lattice formation is a defined feature of Cer-enriched domains generated by the SMase-driven $SM \rightarrow Cer$ conversion.

In addition to the system-specific lattice organization of Cer-enriched domains (Fig. 4), Fig. 5 contrasts further domain properties in both experimental setups. First, Fig. 5 *a* parameterizes the packing of the lipid domains by the nearest distance between adjacent domain borders. Cer-enriched domains of the SMase-driven system (so*lid triangles*) are packed more closely than domains generated by defined mixtures of SM/Cer (*shaded triangles*). At low Cer concentrations (2–5 mol %), the differences are more pronounced than at higher Cer concentration (20–50 mol %). These differences can also be perceived visually in the corresponding picture frames (Fig. 4). Second, the domain size (Fig. 5 *b*)
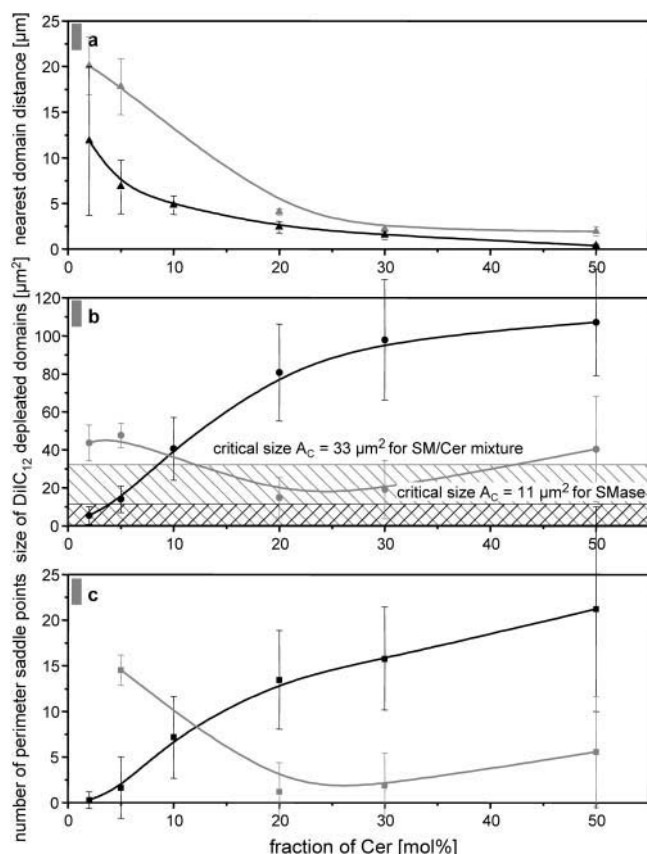
FIGURE 5 Comparative formation of Cer-enriched domains as observed during the time course of the SMase-driven $SM \rightarrow Cer$ conversion (*solid lines* and *symbols*) and in defined mixtures of SM/Cer (*shaded lines* and *symbols*). (*a*) Nearest domain border distances between the Cer-enriched domains. (*b*) Mean size of the DiIC$_{12}$-depleted Cer-enriched domains. The striped regions mark domain sizes which are below the theoretical critical areas for domain instabilities for the SMase-driven system ($A_c \approx 11 \ \mu m^2$, *solid*) and for the mixtures of SM/Cer ($A_c \approx 33 \ \mu m^2$, *shaded*) (see Results And Discussion). (*c*) Mean number of perimeter saddle points. Error bars define SD for the corresponding domain populations. Parameters were calculated for Cer concentrations of 2, 5, 20, 30, and 50 mol % in analogy to the representative picture frames in Fig. 4. For the SMase-driven $SM \rightarrow Cer$ conversion, data points for Cer concentrations of 10 mol % were added for better interpolation of the corresponding β-spline curves.

and shape (Fig. 5 *c*) differ in both experimental systems. For the SMase-driven monolayer, the domain size (*solid circles*) and the number of domain border saddle points (*solid squares*) rise with increasing Cer concentration. For the defined mixtures of SM/Cer instead, both parameters decrease up to Cer concentrations of 20 and 30 mol % before they increase again up to Cer concentrations of 50 mol % (*shaded circles* and s*quares*). At 20 and 30 mol %, the vast majority of these domains adopt circular shapes (compare to Fig. 4, *g* and *j*) with mean domain areas of $A_{20mol\%} = 14.9 \pm 10.6 \ \mu m^2$ and $A_{30mol\%} = 19.1 \pm 14.9 \ \mu m^2$. Since Cer-enriched domains formed freely in the SM/Cer monolayer, Eq. 3 (see Supplementary Material) offers a direct access to Γ: $\Gamma_{SM/Cer,20mol\%} = \mu^2/\lambda = 1/\ln[4 \cdot r_0/(d \cdot e^3)]$ yields 0.163 ± 0.007, respecting

$Z_0 = 3$ for circular Cer-enriched domains (McConnell, 1990, 1991) with an equilibrium radius of $r_0 = 2.18 \pm 0.67 \ \mu m$, and $d = 9.4 \ \text{Å}$ as calculated above. In the same manner, we calculated $\Gamma_{SM/Cer,30mol \ \%} = 0.159 \pm 0.007$ for a Cer-concentration of 30 mol %. The determination of $\Gamma_{SM/Cer}$ from the equilibrium condition allows us in this case to calculate the critical domain area (A_c) which defines when the circular domain shapes become unstable and adopt higher modes m (McConnell, 1990; Vanderlick and Möhwald, 1990). In accordance to the theory of shape transition, circular shapes can only be stable for $A < A_c$ ($A_c = \pi \cdot (d \cdot e^{10/3} \cdot e^{1/\Gamma}/4)^2$), which yields 27.8 ± 11.04 or $37.9 \pm 15.6 \ \mu m^2$ for 20 or 30 mol % Cer, or a mean critical area of $A_c \approx 33 \ \mu m^2$, respectively (see Fig. 5 *b*). For the SM/Cer-mixture, we can actually observe enhanced formation of undulated shapes for domain areas $A > A_c$ (compare Fig. 4, *a*, *d*, and *m*; and Fig. 5 *b*).

As shown, $\Gamma_{SM/Cer}$ is much smaller than $\Gamma_{SMase,t3'} = 0.212$ calculated for the SMase-driven system during the first shape transition (see above). Using the experimental values for μ (determinant parameter for lattice organization and domain size/shape, see Fig. 6 *a* and discussion below), we can calculate the line tension $\lambda = \mu^2/\Gamma$ (the second determinant parameter for domain size/shape). The ratio $\lambda_{SMase}/\lambda_{SM/Cer} = ((6.14 \cdot 10^{-3} \ D/\text{Å}^2)^2/\Gamma_{SMase})/((1.27 \cdot 10^{-3} \ D/\text{Å}^2)^2/\Gamma_{SM/Cer})$ yields 16.5 or 17.5 for Cer-concentrations of 20–30 mol %, indicating much stronger line tension for the SMase-driven system. On the other hand, the ratio $\mu^2_{SMase}/\mu^2_{SM/Cer} = 23.4$ reveals that for the SMase-driven system the repulsive dipolar interaction energies are even more significant. The theory of shape transition allowed us to calculate the critical domain area A_c from the determination of the equilibrium area A_{eq} of the Cer-enriched domains generated by the SM/Cer-mixture. On the other hand, we could calculate the equilibrium domain area A_{eq} from the determination of the critical area A_c at the first shape transition in the SMase-driven system. The value A_{eq} in the SMase-driven system resulted to be approximately twice as high, and A_C even three times as high (see Fig. 5 *b*) as the values determined for the SM/Cer-mixture. According to these values, we can observe that SMase-generated Cer-enriched domains expose higher modes than the corresponding domains of the SM/Cer-mixture (Fig. 4, *g*, *j*, and *m*).

In summary, our results demonstrate that neither morphologic properties nor hexagonal lattice formation of Cer-enriched domains generated by SMase activity can be reproduced by enzyme-free mixtures of SM/Cer. The differences in A_{eq}, A_C, Γ, μ^2, and λ are not only valuable descriptors for the observed domains, they further indicate a different molecular organization of the Cer/SM lipids within the respective Cer-enriched domains. The dipole moment density μ of lipid layers results from the hydrocarbon interior (mainly the terminal C-H bonds of the acyl chains), the headgroups, and the first few water layers adjacent to the interface (Brockman, 1994; Langner and Kubica, 1999). Since Cer-enriched domains are more compact (Fanani et al., 2002),
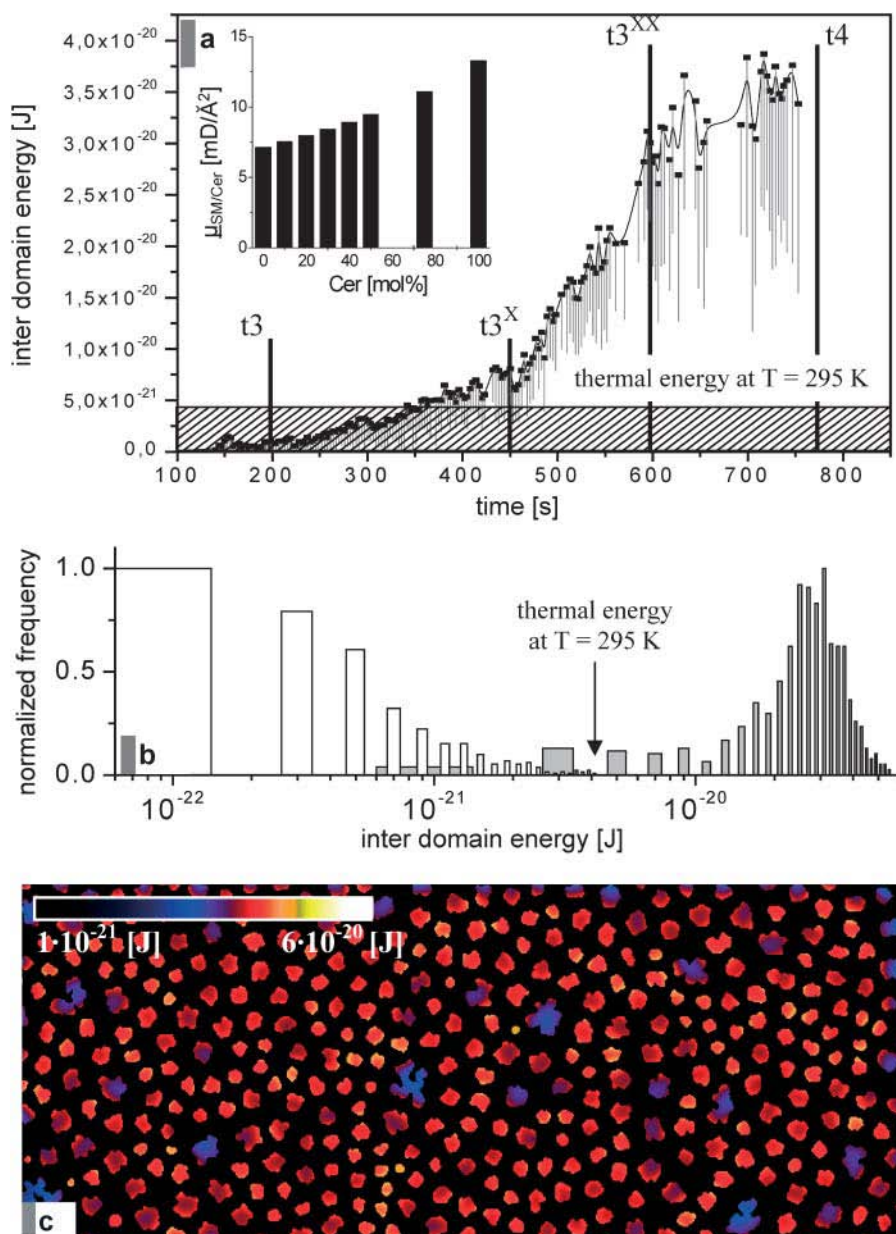
FIGURE 6 Repulsive electrostatic interdomain energies between Cer-enriched domains generated during the time course of SMase-driven $SM \rightarrow Cer$ conversion. (*a*) Mean values of the interdomain energy are connected by β-spline curves. Interdomain energies were calculated for each Cer-enriched domain with respect to the next-nearest-neighbor domain. Error bars define SD. The inset shows dipole moment densities $\mu_{SM/Cer}$ as calculated from the surface potential ΔV measured in pure monolayers and in defined mixtures of SM/Cer at $\Pi = 10$ mN/m. The difference of the dipole moment densities between the Cer-enriched domains in the SM monolayer were calculated by $\mu = \mu_{Cer} - \mu_{SM} = 6.14 \cdot 10^{-3}$ D/Å^2 (see text and Materials and Methods). The striped region marks energies below the thermal energy $W(T) = 4.08 \cdot 10^{-21}$ J ($T = 295$ K). (*b*) Frequency distribution of the repulsive electrostatic domain energies at $t = t3$ (*open columns*) and $t = t3^X$ (*shaded columns*) of the SMase-driven enzymatic reaction. For each domain, the energy was calculated with respect to the first six nearest-neighbor domains. The arrow points out the thermal energy at $T = 295$ K. (*c*) Color-coded presentation of the repulsive dipolar domain energies between lipid domains at $t = t3^X$ of the SMase-driven enzymatic reaction (*x,y*-dimension $= 450 \times 176$ μm). Energies between $1 \cdot 10^{-21}$ J and $6 \cdot 10^{-20}$ J are logarithmically scaled by the color bar. For each domain, the energy was calculated pixelwise with respect to the six nearest-neighbor domains.

ordered, and less fluid than SM layers (Holopainen et al., 1997, 1998), the resultant alignment of the terminal C-H bonds of the acyl chains between adjacent lipids increase the dipole moment density in Cer-enriched domains in comparison to SM-enriched regions (Fanani, 2001). Additionally, the ratio $\mu^2_{SMase}/\mu^2_{SM/Cer} = 23.4$ indicates that the Cer-enriched domains formed by the SMase-driven system are either packed with a higher order, or exclude a higher proportion of remaining SM, than the Cer-enriched domains of the SM/Cer-mixture. Our previous data (Fanani et al., 2002) supports the latter explanation, inasmuch as the total area covered by Cer-enriched domains of the SM/Cer-mixture was significantly larger than the total area covered by SMase-generated, Cer-enriched domains at the same Cer concentration.

Although the surface pattern of the SMase-driven system could not be reproduced by defined mixtures of SM/Cer, similar features have been observed in other lipid systems: nucleation of circular domains, circular growth, and successive second-order shape transitions toward higher modes have also been reported in gel phases in the fluid-gel coexistence regions of phospholipids during compression along pressure-area isotherms (Vanderlick and Möhwald, 1990; McConnell, 1991). Additionally, flower-like Cer-enriched domains with modes between 6 and 7 are formed by Cer$_{24:1}$:DMPC monolayers at surface pressures of 30 and 40 mN/m and at a molar ratio of 20:80 (Holopainen et al., 2001). At a molar ratio of 70:30, the same components formed fractal-like domains at surface pressures between

5 and 40 mN/m. Unfortunately, the authors did not discuss nor provide a quantitative evaluation of the lateral domain organization.

Reciprocal action among interdomain energy, morphologic transitions, and lateral organization of Cer-enriched domains

Repulsive interactions at the molecular (lipid) or the supramolecular (domain) level in combination with two-dimensional phase immiscibility can provide important driving forces for surface organization. One example at the molecular level is the regular distribution of sterols in phospholipid bilayers on the basis of the lipid superlattice model (Somerharju et al., 1985; Virtanen et al., 1988, 1995). According to this model, lipid components with a different cross-sectional area than the surrounding lipids introduce lateral tensions that are minimized when the components adopt a regular distribution inside the matrix (Somerharju et al., 1999). Among other effects, regular lipid distributions have been proposed to control membrane lipid composition and asymmetry through the regulation of membrane-active enzymes. In this context, molecular superlattices formed by cholesterol have shown to regulate the metabolic activity for phosphohydrolytic enzymes like PLA_2 (Chong and Sugár, 2002; Liu and Chong, 1999). In further studies, PLA_2-activity has been affected by SMase-generated Cer in a surface pressure-dependent and molecular packing-dependent manner (Fanani and Maggio, 1997, 1998). Despite the identical hydrocarbon moieties of SM and Cer used in this study, SM and Cer are practically immiscible at a surface pressure of $\Pi = 10$ mN/m, and SM adopts a liquid-expanded state whereas Cer forms a very condensed monolayer (Fanani et al., 2002). Under these conditions, the mean molecular area of SM is 84 Å^2 whereas Cer occupies 51 Å^2 and resembles a molecular geometry of an inverted cone due to the small size of its polar headgroup. These geometrical features lead to lateral tensions that induce changes of the interfacial curvature or topology (Kolesnick et al., 2000) and have even been found to induce asymmetrical bilayer budding in SM liposomes on a micrometer scale (Holopainen et al., 2000). Nevertheless, regular, lattice-like Cer distributions in lipid membranes have not yet been observed and all available publications hint at the formation of segregated Cer-enriched lateral domains (Holopainen et al., 1997, 1998; Szabo et al., 2004) or Cer-enriched membrane platforms (Gulbins et al., 2004). Our own findings that SM and Cer are mutually immiscible (Fanani et al., 2002) also contradict a possible regular Cer distribution. As shown in Figs. 3 and 4, SMase-generated, Cer-enriched domains form superlattices that are not equivalent to the molecular superlattices discussed above. But, following the concepts of entropy, regular patterns intrinsically possess a higher content of information than irregular patterns, and can convey information between different scales via the underlying lattice forces. Although

molecular superlattices close the communication gap between single lipid headgroup distances (nanometer scale) up to a few lipid headgroup distances of <10 nm (Somerharju et al., 1999), domain superlattices actually reach the 10-μm scale via repulsive interdomain energies resulting from the intrinsic dipole moment density μ (Fig. 3 a and Fig. 6).

Under certain assumptions, the dipole moment density μ_X of a lipid class X in a monolayer perpendicular to the air-water interface can be calculated from the surface dipole potential ΔV (Brockman, 1994; Cseh and Benz, 1999). We determined ΔV in pure monolayers of SM and Cer, and in defined mixtures of SM/Cer at $\Pi = 10$ mN/m (Fanani, 2001). We obtained $\Delta V = 270, 285, 300, 318, 336, 357, 419,$ and 500 mV (maximum mean plus SE, ± 30 mV) at 0, 10, 20, 30, 40, 50, 75, and 100 mol % [Cer]. Since SM and Cer are practically immiscible, these experimental values are within 10% of the values calculated for fully immiscible monolayers. From these values and the corresponding mean molecular areas, we calculated the dipole moment densities $\mu_{SM/Cer}$: $7.16 \cdot 10^{-3}$, $7.55 \cdot 10^{-3}$, $7.97 \cdot 10^{-3}$, $8.43 \cdot 10^{-3}$, $8.93 \cdot 10^{-3}$, $9.47 \cdot 10^{-3}$, $11.1 \cdot 10^{-3}$, and $13.3 \cdot 10^{-3}$ D/Å^2 (see Fig. 6 a, $inset$). Interestingly, $\mu_{SM/Cer}$ rises slowly when Cer concentrations increase from 0 to 50 mol %, whereas a stronger increase can be detected between 50 and 100 mol %. Our observation agrees with data published for C24:1-ceramide in DMPC monolayers, especially at low surface pressures of 5 and 15 mN/m (Holopainen et al., 2001). From $\mu_{SM/Cer}$, the difference of the dipole moment densities between the pure SM and the pure Cer phase can be calculated ($\mu = \mu_{Cer} - \mu_{SM} = 6.14 \cdot 10^{-3}$ D/Å^2) and the interdomain energy W can be derived (Eq. 1).

Fig. 6 shows the repulsive electrostatic interdomain energies between Cer-enriched domains generated during the time course of SMase-driven $SM \rightarrow Cer$ conversion. The average repulsive domain energy is plotted as a function time in Fig. 6 a. In each frame, the energy was calculated for every domain with respect to its nearest-neighbor. Directly after the spontaneous domain formation ($t3$), the average repulsive domain energy appears small in comparison to the thermal energy. But, as the population statistics in Fig. 6 b reveals, the energies of many of the domains are already high enough to enforce lateral reorganization on a micromolar scale (see Fig. 3 and discussion below). At this stage of the reaction, the distance between the Cer-enriched domains is the determinant factor for the interdomain energies. Therefore, repulsive forces primarily act upon domains which are in close proximity to each other (see Fig. 3 c). At $t > t3$, the interdomain energies increase steadily concomitant to the growth of the Cer-enriched domain areas (Fig. 1), and the gradual organization of the domains into hexagonal lattices (Figs. 3 and 4). At $t > t3^X$, the domains become trapped by the hexagonal lattice forces (Fig. 3), which impede further displacements or reorganization, which, in consequence, results in a much stronger increase of the interdomain repulsive energies (Fig. 6 a) parallel to the unaltered growth

of the domains (Fig. 1). This point demonstrates clearly that the lateral domain organization directly controls the variation of the electrostatic field generated by the dipole moments of domain-forming lipids: the hexagonal lattice structure amplifies the potential to regulate the electrostatic field by the size of the Cer-enriched domains by a factor of ~ 5. At $t > t3^{XX}$, the increase of the interdomain energy slows down again to a rate similar to the one observed at $t < t3^X$. This rate decrease coincides with the manifestation of the second morphologic transition from star-like shapes to higher border undulations at $t3'''$ (Fig. 2 a) and occurs despite the unaltered growth of the lattice-bound domains (Figs. 1 a and 3 a). Since the domain shape determines the interdomain geometry (see r_b at $t3^{XX}$ in Fig. 3 a), shape transitions have a direct impact on the electrostatic field and the interdomain energy (Eq. 1). In conclusion, domain size, domain morphology, and the lateral domain organization together determine the interdomain energy in a defined manner. All three features define a SMase-driven, specific surface architecture, which directly controls the electrostatic field and thus the communication/interaction between the Cer-enriched domains.

Fig. 6 b contains the frequency distributions of the interdomain energies at $t3$ (end of spontaneous domain formation) and at $t3^X$ (hexagonal lattice organization). In contrast to Fig. 6 a, the energy for every domain was calculated with respect to the first six nearest-neighbor domains. In general, the lateral movement of the Cer-enriched domains is defined by the interdomain energy and the thermal energy $W(T) = k_b T$ which drives random Brownian motion. At room temperature ($T = 295$ K), the thermal energy yields $4.08 \cdot 10^{-21}$ J. At $t3$, >20% of the Cer-enriched domains possess interdomain energies $>10^{-21}$ J. These energies are high enough to compete with the thermal energy and to direct random movement toward an ordered lattice organization (see hgd-values in Fig. 3 a). Additionally, the mean domain center distance r_c increases directly after nucleation, which shows that repelling forces act upon a significant number of domains. At $t3^X$, the mean interdomain energy outnumbers the thermal energy by a factor of 10, rigorously trapping the domains inside the lattice structure. A direct visual codification of the distribution of the interdomain energies on the Cer-enriched domains is given in Fig. 6 c. The image shows domains that contribute to the calculation of the frequency distribution of the interdomain energies in Fig. 6 b at $t3^X$. Nearly all domains provide increased energies distributed homogeneously around their borders. It can further be observed how larger Cer-enriched domains define local boundary traps, impeding a perfect hexagonal lattice organization among all domains. In turn, these boundary traps themselves define centers for recognizable circular super-superstructures of the surrounding domains. The strong electrostatic field gradients in such traps constitute electrostatic potential attractors or repulsive regions for laterally diffusing molecules. In contrast, the smaller dipole density differences determined in defined SM/Cer-mixtures at Cer concentrations between 0 and 50 mol %

do not lead to hexagonal lattice formation (Fig. 4). It is important to consider that the electrostatic interdomain energy depends on μ^2, which implies major amplification for small variations of μ and explains why SM/Cer-mixtures do not organize laterally. In conclusion, the energetic evaluations based on experimentally determined dipole moment densities are in agreement with the observed differences in the domain organization in both experimental systems.

It has been correctly remarked that the domain topography in monolayer films corresponds to metastable conditions that may not reach equilibrium for days (McConnell, 1991). On the other hand, it is well known that structural, diffusional, and kinetic information can be stored and transmitted from the molecular to the supramolecular level by a large variety of spontaneous self-organized structures in systems that are continuously evolving, far-off, any equilibrium condition (Nicolis and Prigogine, 1977; Peacocke, 1989). Our results suggest that the SMase-sculptured surface topography represents a condition far from equilibrium. During lipolysis, the generation of Cer with a kinetic constant of $k_{cat} \approx 10^3$ s^{-1} (Fanani and Maggio, 2000) is not sufficient to explain the formation of non-equilibrium domains, inasmuch as lateral lipid diffusion rates take place on a scale of several μm s^{-1} and exchange frequencies with the respective nearest-neighbor lipids occur at $\sim 10^7$ s^{-1}. Under these circumstances, a first-generated, freely diffusing, and immiscible Cer molecule is not available for clustering with the subsequently generated Cer. In consequence, the formation of Cer-enriched domains would be a purely diffusion-controlled process, with features similar to those of SM/Cer-mixtures. Since this is not the case, we must postulate an additional property of the metabolizing enzyme SMase, or an influence of the fluorescent probe DiIC$_{12}$, or defined interactions with the second product of the $SM \rightarrow Cer$ conversion, phosphocholine. Due to its hydrophilic properties the concentration of this charged residue in the aqueous subphase at the end of the reaction remains below 2 nM; at this concentration it is very unlikely that phosphocholine contributes significantly to the observed surface architecture. An artifact produced by the chemically highly inert fluorescent probe DiIC$_{12}$ (Härtel et al., 2002) can also be excluded extensively, since Holopainen et al. (1998) detected SMase-induced Cer aggregation indirectly with two alternative fluorescent techniques: 1), diphenylhexatriene (DPH) sensed a decreased rotational diffusion by increased fluorescence polarization; and 2), pyrene-labeled Cer analogs showed characteristic excimer emission and therefore close vicinity of the Cer components. We rather suspect a new, explicit property of the metabolizing enzyme SMase to be responsible for the observed pattern. The enzyme, once attached and activated on the interface, could generate a lateral region with defined lipid dynamics, composition, and significantly lowered diffusion coefficients through protein-specific surface interactions of the type described by May et al. (2000). It could also be possible that metabolized Cer molecules are retained near the active

site and interwoven with the subsequent Cer molecule before they are released to the lipid layer. We are currently performing experiments that concentrate on the precise location of SMase in the monolayer. On the other hand, the enzyme-free mixtures of SM/Cer represent more equilibrated interfaces. We controlled whether the surface topography observed in the SMase-driven system is induced by SMase itself by adding SMase to the enzyme-free SM film in the presence of 60 mM EDTA-Na$_2$. In the absence of Mg^{2+} ions, the SMase activity is totally inhibited. We could not observe changes in the surface topography in the presence of inactive enzyme, and therefore exclude that structure-related properties of the protein itself induce the SMase-specific pattern. Furthermore, we also injected EDTA-Na$_2$ into the reaction subphase at a specific point of the ongoing lipolysis ($t = 400$ s, 25 mol % Cer). Here, the evolution of the topographic pattern was simply detained at the stage of first-order domain branching.

The synopsis shown in Fig. 7 covers the entire period of the SMase-driven $SM \rightarrow Cer$ conversion in SM monolayers. Within this timeframe, the total surface area covered by Cer-enriched domains increases in a linear manner (Fig. 7, *upper plot*), and a total of eight well-defined transitions in the lateral organization or the domain morphology can be detected (Fig. 7, *lower horizontal bar graphs* and *shaded arrows*). The time-course of the reaction shows that those transitions precede or are concomitant to defined changes of the reaction kinetics, underlying their correlation and crosstalk to the catalytic features of the enzymatic $SM \rightarrow Cer$ conversion at the interface. In the SMase-driven experiment,

the hexagonal domain lattice formation occurs isochronally to the morphologic transitions (Fig. 7). When Cer-enriched domains adopt a primarily hexagonal lattice organization ($t3^X$), they are trapped by isotropically distributed electrostatic energy around their borders (Fig. 6 *b*). The radial expansion of the domain branches can no longer be compensated by a lateral retraction of the domains that accelerates the decrease of the border distances r_b between $t3^X$ and $t3^{XX}$. The accelerated decrease of r_b in turn leads to a further increase of the dipolar repulsion energy $W \sim 1/r_b^3$, which further strengthens the domain lattice organization. Subsequently, the detection of the second border undulation at $t3'''$ is followed almost instantly by a slower decrease of the domain border distances and a slower increase of the interdomain energies at $t3^{XX}$. The consecutive splicing of the branches deviates the radial expansion of the domains, which explains why r_b diminishes more slowly at $t > t3^{XX}$. When we consider the increased electrostatic energy W at the domain mode apexes at $t3^X$ (Fig. 6 *b*), it is possible that the splicing of the apexes itself is the direct consequence of a further concentration of the repulsive energy $W \sim 1/r_b^3$. At $t > t3''$, the apexes of the Cer-enriched domains expand preferentially into the domain interspaces and form a toothed wheel-like organization that physically indents the rigid domains (Fig. 1 *e* and Fig. 7). Strong electrostatic repulsion within an increasingly crowded lattice then leads to an overall change of the surface dynamics: lateral monolayer flow and rotationally coupled movements of the domains are established (visual observation of the monolayer dynamics in the image time-series at $t > t3^{XX}$, see Supplementary Material,
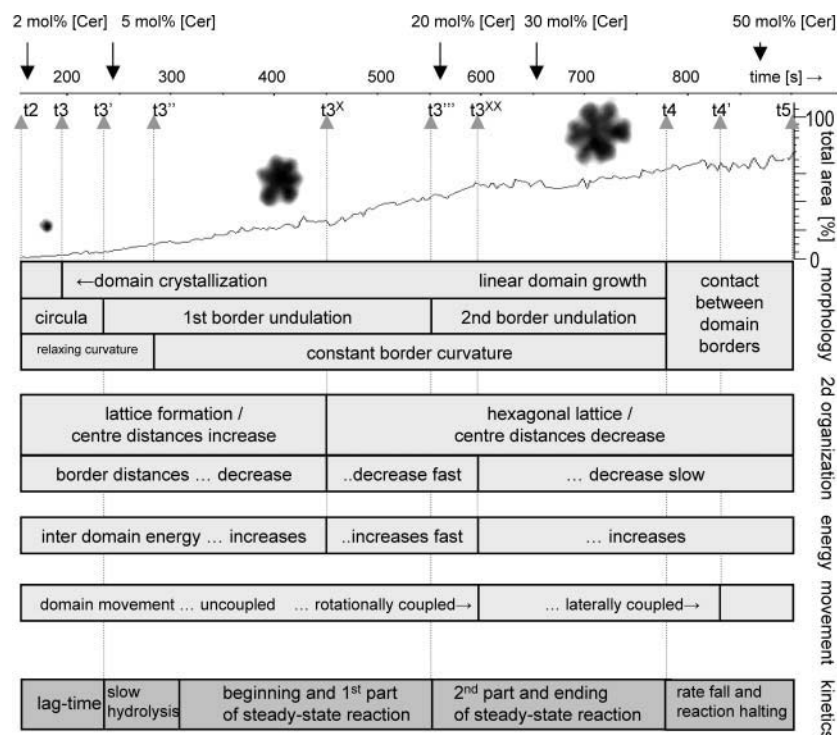

FIGURE 7 Synopsis of multiple stages in the lipid domain organization induced by SMase-driven $SM \rightarrow Cer$ conversion. The timescale in the upper part of the diagram covers the entire period of the pseudo zero-order kinetics of the enzymatic conversion, which starts directly after the lag time ($t2$) and lasts until the constant $SM \rightarrow Cer$ conversions cease at $t > t5$. The total area covered by growing Cer-enriched domains is plotted in percent of the total monolayer area. Representative examples depict domain morphologies at three different stages of the enzymatic reaction. On top of the timescale, solid arrows indicate Cer concentrations used to compare defined mixtures of SM/Cer to the SMase-driven system (Figs. 4 and 5). Below the timescale, shaded arrows mark the entire set of SMase-induced transitions, which are listed in the lower bar charts: the first horizontal bar chart summarizes morphologic transitions of the Cer-enriched domains (Figs. 1 and 2); the second chart focuses on the domain lattice organization (Figs. 3 and 4); the third chart indicates changes of the interdomain energy (Fig. 6); the fourth chart marks the transition of uncoupled domain movement to directly coupled domain movement; and the fifth, lower dark-shaded chart shows the different kinetic steps of the enzymatic reaction as determined by the surface barrier movement (Fig. 1 *a*, *inset*).

SMase.avi and *SMaseMask.avi*). Finally, at $t > $ t4′, the increasing interaction between the domain borders leads to a viscous coupling of lateral movement of the domains, which occurs directly after the point where domain borders can no longer be separated on the selected scale. As we have shown, morphology, lattice organization, lateral dynamics, and inter-domain energy are interconnected properties of the SMase-generated, Cer-enriched domains and differ substantially from the spontaneously formed topography of the SM/Cer-mixture. In consequence, the SMase-driven system generates defined non-equilibrium states with a high potential to store and communicate information on multiple scales. The SMase-specific control of non-equilibrium surface topographies, with direct influence on physicochemical membrane properties on a micromolar scale, adds a new perspective to the possible role of lipolytic enzymes in cell signaling.

Possible implications for studies of lipid properties in model systems and in cellular signaling

Apart from experimental boundary conditions like temperature, pH, or ionic strength of the subphase, lateral interactions and morphological features of lipid domains formed by membrane lipids depend on the headgroup characteristics (Maggio et al., 2004) and on the specific acyl-chain properties such as acyl-chain length and the degree of saturation (Holopainen et al., 2001). Our data add further perspectives to this field: the enzyme *B. cereus* SMase generates lateral domains of defined molecular composition that determine specific surface morphologies, lateral organization patterns, and concomitant interaction potentials on various scales. This statement might not seem too surprising considering that different compression or expansion velocities in lipid monolayers lead to different (metastable) domain organizations (e.g., Helm and Möhwald, 1988). The novelty is that SMase converts SM to Cer at a constant surface pressure—and that it produces substantially different layer properties than any of the defined mixtures of SM/Cer (with the same composition) under similar boundary conditions. Thus, the role of the phosphohydrolytic enzyme goes far beyond a simple biochemical $SM \rightarrow Cer$ conversion, providing laterally immiscible lipid domains with the capacity to mediate and transduce information at the membrane level. As previously shown, Cer-enriched domains generated by SMase and SM/Cer-mixtures cover different total monolayer areas, which hints toward different domain-intrinsic SM/Cer compositions (Fanani et al., 2002). Our new data show that SMase accounts for a specific out-of-equilibrium domain-intrinsic composition, packing, and/or orientation of the molecular dipole moments perpendicular to the air/water interface. Both molecular packing and orientation on a nanomolar scale define the local dipole moment density μ, which leads

to the discussed effects on three scales: 1), the domain-intrinsic shape-transition on a micromolar scale; 2), the formation of superstructures or lateral domain organization on a scale of ~10 μm; and 3), the formation of super-superstructures on a scale of ~50–100 μm.

It is widely accepted that transmembrane lipid asymmetry in biological membranes is constituted, maintained, and countermanded actively, triggering a manifold of inter- and intracellular signal cascades (Sims and Wiedmer, 2001; Boon and Smith, 2002). Examples are phosphatidylserine-externalization during apoptosis (Fadok et al., 1992), or the synchronous SM internalization that mediates SMase-driven $SM \rightarrow Cer$ conversion and successive morphological membrane alterations on a three-dimensional level (Tepper et al., 2000). We suggest here that out-of-equilibrium states and information transduction by actively generated local changes of lipid composition must also be considered on the lateral membrane level. Our study clearly shows that there is high content of information in the local topographic features and in the dynamics of an actively changing surface, so great care should be taken when attempting to mimic membrane properties with equilibrium model systems (Maggio et al., 1994; Maggio, 1966; Montes et al., 2002). Self-agglomerated lateral domain/raft formation on micromolar scales by mixtures of cholesterol, SM, or phosphatidylcholine has recently been observed in giant liposomes (Devaux and Morris, 2004). The concept of lateral out-of-equilibrium states could explain why rafts in natural membranes have only been observed on nanometer scales (Munro, 2003). SMase-driven agglomeration and regulation of ion channels at different stages of apoptosis has recently been discussed by Szabo et al. (2004). Lateral out-of-equilibrium states generally open new perspectives for domain-related modulation of membrane enzymatic activity and structural signaling, and our findings of a Cer-domain-specific control of the dipolar field strength should be considered as a possible regulatory mechanism for channel conductance against the background of the surface-charge hypothesis (Moczydlowski et al., 1985; Park et al., 2003). Different pH- or Mg^{2+}-dependent isoforms of SMase could lead to enzyme-specific, Cer-enriched domains with defined structural-functional properties and signaling patterns from nanometer to micromolar scales.

CONCLUSIONS

In summary, our work gives a precise description of biocatalytic-topographic codes that exchange information between molecular level and supramolecular, long-range patterns. Although the local molecular mechanisms leading to the SMase-controlled surface topography are beginning to emerge, further studies will be needed to unmask the remaining questions about SMase-related signal transduction via explicit membrane architecture.

APPENDIX: DEFINITIONS

A, area.

A_C, critical domain area.

A_{eq}, equilibrium domain area.

Cer, ceramide.

μ_{Cer}, dipole moment density of Cer.

$\mu = \mu_{Cer} - \mu_{SM}$, dipole moment density difference.

$DiIC_{12}$, 1,1′-didodecyl-3,3,3′,3′-tetramethylindocarbocyanine perchlorate.

DPH, diphenylhexatriene.

E, electrostatic field (W).

ε, relative amplitude of undulation.

hgd, highest gap distance.

I, intensity.

IDL, interactive data language.

λ, line tension.

LC, liquid-condensed.

LE, liquid-expanded.

m, undulation mode.

P, perimeter.

r_b, domain border distance.

r_c, domain center distance.

SM, sphingomyelin.

μ_{SM}, SM perpendicular to the water surface.

SMase/s, sphingomyelinase/s.

Π, surface pressure.

SUPPLEMENTARY MATERIAL

An online supplement to this article can be found by visiting BJ Online at http://www.biophysj.org.

REFERENCES

Basañez, G., G. D. Fidelio, F. M. Goñi, B. Maggio, and A. Alonso. 1996. A twofold inhibitory effect of glycosphingolipids on phospholipase C-promoted fusion of lipidic vesicles. *Biochemistry*. 35:7506–7513.

Boon, J. M., and B. D. Smith. 2002. Chemical control of phospholipid distribution across bilayer membranes. *Med. Res. Rev*. 22:251–281.

Bianco, I. D., G. D. Fidelio, and B. Maggio. 1989. Modulation of phospholipase A_2 activity by neutral and anionic glycosphingolipids in monolayers. *Biochem. J*. 258:95–99.

Bianco, I. D., G. D. Fidelio, and B. Maggio. 1990. Effect of sulfatide and gangliosides on phospholipase C and phospholipase A2 activity. A monolayer study. *Biochim. Biophys. Acta*. 1026:179–185.

Bianco, I. D., G. D. Fidelio, R. K. Yu, and B. Maggio. 1991. Degradation of dilauroylphosphatidylcholine by phospholipase A_2 in mixed monolayers containing glycosphingolipids. *Biochemistry*. 30:1709–1714.

Brockman, H. L. 1994. Dipole potential of lipid membranes. *Chem. Phys. Lipids*. 73:57–79.

Carrer, D. C., and B. Maggio. 1999. Phase behavior and molecular interactions in mixtures of ceramide with dipalmitoyl phosphatidylcholine. *J. Lipid Res*. 40:1978–1989.

Carrer, D. C., S. Härtel, H. L. Monaco, and B. Maggio. 2003. Ceramide modulates the lipid membrane organization at molecular and supramolecular levels. *Chem. Phys. Lipids*. 122:147–153.

Castleman, K. R. Digital Image Processing. Prentice Hall, Englewood Cliffs, NJ. Chapt. 19.

Chong, P. L.-G. 1994. Evidence for regular distribution of sterols in liquid-crystalline phosphatidylcholine bilayers. *Proc. Natl. Acad. Sci. USA*. 91: 10969–10973.

Chong, P. L.-G., and I. P. Sugàr.2002. Fluorescence studies of lipid regular distribution in membranes. *Chem. Phys. Lipids*. 116:153–175.

Cseh, R., and R. Benz. 1999. The adsorption of phloretin to lipid monolayers and bilayers cannot be explained by Langmuir adsorption isotherms alone. *Biophys. J*. 74:1399–1408.

Devaux, P. F., and R. Morris. 2004. Transmembrane asymmetry and lateral domains in biological membranes. *Traffic*. 5:241–246.

Exton, J. H. 1994. Phosphatidylcholine breakdown and signal transduction. *Biochim. Biophys. Acta*. 1212:26–42.

Fadok, V. A., D. R. Voelker, P. A. Campbell, J. J. Cohen, D. L. Bratton, and P. M. Henson. 1992. Exposure of phosphatidylserine on the surface of apoptotic lymphocytes triggers specific recognition and removal by macrophages. *J. Immunol*. 148:2207–2216.

Fanani, M.-L. 2001. Supramolecular modulation of sphingomyelinase activity in biointerfaces. PhD thesis. Departamento de Quimica Biológica, Facultad de Ciencias Químicas, Universidad Nacional de Córdoba, Córdoba, Argentina.

Fanani, M. L., and B. Maggio. 1997. Mutual modulation of sphingomyelinase and phospholipase A_2 activities against mixed lipid monolayers by their lipid intermediates and glycosphingolipids. *Mol. Membr. Biol*. 14: 25–29.

Fanani, M. L., and B. Maggio. 1998. Surface pressure-dependent cross-modulation of sphingomyelinase and phospholipase A_2 in monolayers. *Lipids*. 33:1079–1087.

Fanani, M. L., and B. Maggio. 2000. Kinetic steps for the hydrolysis of sphingomyelin by *Bacillus cereus* sphingomyelinase in lipid monolayers. *J. Lipid. Res*. 41:1832–1840.

Fanani, M. L., S. Hartel, R. G. Oliveira, and B. Maggio. 2002. Bidirectional control of sphingomyelinase activity and surface topography in lipid monolayers. *Biophys. J*. 83:3416–3424.

Freeman, H. 1970. Boundary encoding and processing. *In* Picture Processing and Psychopictorics. B.S. Lipkin and A. Rosenfeld, editors. Academic Press, New York. 241–266.

Gatt, S. 1999. Studies of sphingomyelin and sphingomyelinases. *Chem. Phys. Lipids*. 102:45–53.

Grainger, D. W., A. Reichert, H. Ringsdorf, and C. Salesse. 1990. Hydrolytic action of phospholipase A_2 in monolayers in the phase transition region: direct observation of enzyme domain formation using fluorescence microscopy. *Biochim. Biophys. Acta*. 1023:365–379.

Gulbins, E., S. Dreschers, B. Wilker, and H. Grassme. 2004. Ceramide, membrane rafts and infections. *J. Mol. Med*. 82:357–363.

Hannun, Y. A., and C. Luberto. 2000. Ceramide in the eukaryotic stress response. *Trends Cell. Biol*. 10:73–80.

Härtel, S., S. Tikhonova, M. Haas, and H. Dile. 2002. Membrane-sensitive fluorescent dyes for applications in fluorescence microscopy. *J. Fluoresc*. 12:465–479.

Härtel, S., M. Zorn-Kruppa, S. Tikhonova, P. Heino, M. Engelke, and H. Diehl. 2003. Staurosporine-induced apoptosis in human cornea epithelial cells in vitro. *Cytometry*. 8:15–23.

Heinz, D. W., L. O. Essen, and R. L. Williams. 1998. Structural and mechanistic comparison of prokaryotic and eukaryotic phosphoinositide-specific phospholipase C. *J. Mol. Biol*. 275:635–650.

Helm, C. A., and H. Möhwald. 1988. Equilibrium and nonequilibrium features determining superlattices in phospholipid monolayers. *J. Phys. Chem.* 92:1262–1266.

Holopainen, J. M., J. Y. Lehtonen, and P. K. Kinnunen. 1997. Lipid microdomains in dimyristoylphosphatidylcholine-ceramide liposomes. *Chem. Phys. Lipids.* 88:1–13.

Holopainen, J. M., M. Subramanian, and P. K. Kinnunen. 1998. Sphingomyelinase induces lipid microdomain formation in a fluid phosphatidylcholine/sphingomyelin membrane. *Biochemistry.* 37: 17562–17570.

Holopainen, J. M., M. I. Angelova, and P. K. Kinnunen. 2000. Vectorial budding of vesicles by asymmetrical enzymatic formation of ceramide in giant liposomes. *Biophys. J.* 78:830–838.

Holopainen, J. M., H. L. Brockman, R. E. Brown, and P. K. Kinnunen. 2001. Interfacial interactions of ceramide with dimyristoylphosphatidyl-choline: impact of the N-acyl chain. *Biophys. J.* 80:765–775.

Honger, T., K. Jorgensen, D. Stokes, R. L. Biltonen, and O. G. Mouritsen. 1997. Phospholipase A_2 activity and physical properties of lipid-bilayer substrates. *Methods Enzymol.* 286:168–190.

Huang, H. W., E. M. Goldberg, and R. Zidovetzki. 1999. Ceramides modulate protein kinase C activity and perturb the structure of phosphatidylcholine/phosphatidylserine bilayers. *Biophys. J.* 77:1489–1497.

Jain, M. K., and O. Berg. 1989. The kinetics of interfacial catalysis by PLA_2 and regulation of interfacial activation: hopping versus scooting. *Biochim. Biophys. Acta.* 1002:127–156.

Jungner, M., H. Ohvo, and P. Slotte. 1997. Interfacial regulation of bacterial sphingomyelinase activity. *Biochim. Biophys. Acta.* 1344:230–240.

Kolesnick, R. N., F. M. Goñi, and A. Alonso. 2000. Compartmentalization of ceramide signaling: physical foundations and biological effects. *J. Cell. Physiol.* 184:285–300.

Krönke, M. 1999. Biophysics of ceramide signaling: interaction with proteins and phase transition of membranes. *Chem. Phys. Lipids.* 101: 109–121.

Langner, M., and K. Kubica. 1999. Electrostatics of lipid surfaces. *Chem. Phys. Lipids.* 101:3–35.

Levade, T., and J. P. Jaffrézou. 1999. Signaling sphingomyelinases: which, where, how and why? *Biochim. Biophys. Acta.* 1438:1–17.

Liu, F., and P. L. G. Chong. 1999. Evidence for a regulatory role of cholesterol superlattices in the hydrolytic activity of secretory phospho-lipase A_2 in lipid membranes. *Biochemistry.* 38:3867–3873.

Maggio, B. 1994. The surface behavior of glycosphingolipids in bio-membranes. A new frontier of molecular ecology. *Progr. Biophys. Mol. Biol.* 62:55–117.

Maggio, B. 1966. Control by ganglioside GD1a of PLA_2 activity through modulation of the lamellar hexagonal (H^{II}) phase transition. *Mol. Membr. Biol.* 13:109–112.

Maggio, B., I. D. Bianco, G. G. Montich, G. D. Fidelio, and R. K. Yu. 1994. Regulation by gangliosides and sulfatides of phospholipase A_2 activity against dipalmitoyl- and dilauroylphosphatidylcholine in small unilamellar bilayer vesicles and mixed monolayers. *Biochim. Biophys. Acta.* 1190:137–148.

Maggio, B. 1999. Modulation of phospholipase A_2 by electrostatic fields and dipole potential of glycosphingolipids in monolayers. *J. Lipid Res.* 40:930–939.

Maggio, B., D. C. Carrer, M. L. Fanani, R. G. Oliveira, and C. M. Rosetti. 2004. Interfacial behavior of glycosphingolipids and related sphingo-lipids. *Curr. Op. Colloid Interface Sci.* 8:448–458.

May, S., D. Harries, and A. Ben-Shaul. 2000. Lipid demixing and protein-protein interactions in the adsorption of charged proteins on mixed membranes. *Biophys. J.* 79:1747–1760.

McConnell, H. M. 1990. Harmonic shape transitions in lipid monolayer domains. *J Phys. Chem.* 94:4728–4731.

McConnell, H. M. 1991. Structures and transitions in lipid monolayers at the air water interface. *Annu. Rev. Phys. Chem.* 42:171–195.

McConnell, H. M. 1993. Elementary theory of Brownian motion of trapped domains in lipid monolayers. *Biophys. J.* 64:577–580.

Moczydlowski, E., O. Alvarez, C. Vergara, and R. Latorre. 1985. Effect of phospholipid surface charge on the conductance and gating of a Ca^{2+}-activated K^+ channel in planar lipid bilayers. *J. Membr. Biol.* 83:273–282.

Montes, L. R., M. B. Ruiz-Arguello, F. M. Goni, and A. Alonso. 2002. Membrane restructuring via ceramide results in enhanced solute efflux. *J. Biol. Chem.* 277:11788–11794.

Montich, G. G., M. Bustos, B. Maggio, and F. A. Cumar. 1985. Micropolarity of interfaces containing anionic and neutral glycosphin-golipids as sensed by merocyanine 540. *Chem. Phys. Lipids.* 38:319–326.

Muderhwa, J. M., and H. L. Brockman. 1992. Lateral lipid distribution is a major regulator of lipase activity. Implications for lipid-mediated signal transduction. *J. Biol. Chem.* 267:24184–24192.

Munro, S. 2003. Lipid rafts: elusive or illusive? *Cell.* 115:377–388.

Nassoy, P., W. R. Birch, D. Andelman, and F. Rondelez. 1996. Hydro-dynamic mapping of two-dimensional electric fields in monolayers. *Phys. Rev. Lett.* 76:455–458.

Nicolis, G., and I. Prigogine. 1977. Self-organization in non-equilibrium systems. *In* Part IV, Control Mechanisms in Chemical and Biological Systems. Wiley-Interscience, New York. 339–429.

Park, J. B., H. J. Kim, P. D. Ryu, and E. Moczydlowski. 2003. Effect of phosphatidylserine on unitary conductance and Ba^{2+} block of the BK Ca^{2+}-activated K^+ channel: re-examination of the surface charge hypothesis. *J. Gen. Physiol.* 121:375–397.

Peacocke, A. R. 1989. The physical chemistry of biological organization. *In* Part II, Kinetic Interpretation of Living Systems. Clarendon Press/Oxford University Press, New York. 111–238.

Peitgen, H. O., H. Jürgens, and D. Saupe. 1998. The Principles of Chaos. Fractals. Rowohld GmbH, Hamburg, Germany. 129.

Ransac, S., H. Moreau, C. Riviere, and R. Verger. 1991. Monolayer techniques for studying phospholipase kinetics. *Methods Enzymol.* 197: 49–65.

Roberts, M. F. 1996. Phospholipases: structural and functional motifs for working at an interface. *FASEB J.* 10:1159–1172.

Ruiz-Arguello, M. B., G. Basanez, F. M. Goni, and A. Alonso. 1996. Different effects of enzyme-generated ceramides and diacylglycerols in phospholipid membrane fusion and leakage. *J. Biol. Chem.* 271:26616–26621.

Ruiz-Arguello, M. B., M. P. Veiga, J. L. Arrondo, F. M. Goni, and A. Alonso. 2002. Sphingomyelinase cleavage of sphingomyelin in pure and mixed lipid membranes. Influence of the physical state of the sphingolipid. *Chem. Phys. Lipids.* 114:11–20.

Saéz-Cirión, A., G. Basañez, G. D. Fidelio, F. M. Goñi, B. Maggio, and A. Alonso. 2000. Sphingolipids(galactosylceramide and sulfatide) in lamellar-hexagonal phospholipid phase transitions and in membrane fusion. *Langmuir.* 23:8958–8963.

Szabo, I., C. Adams, and E. Gulbins. 2004. Ion channels and membrane rafts in apoptosis. *Pflugers Arch.* 448:304–312.

Sims, P. J., and T. Wiedmer. 2001. Unraveling the mysteries of phospholipid scrambling. *Thromb. Haemostat.* 86:266–275.

Somerharju, P. J., J. A. Virtanen, K. K. Eklund, P. Vainio, and P. K. J. Kinnunen. 1985. 1-Palmitoyl-2-pyrenedeanoyl glycerophospholipids as membrane probes: evidence for regular distribution in liquid-crystalline phosphatidylcholine bilayers. *Biochemistry.* 24:2773–2781.

Somerharju, P., J. A. Viranen, and K. H. Cheng. 1999. Lateral organization of membrane lipids. The superlattice view. *Biochim. Biophys. Acta.* 1440:32–48.

Spink, C. H., M. D. Yeager, and G. W. Feigenson. 1990. Partitioning behavior of indocarbocyanine probes between coexisting gel and fluid phases in model membranes. *Biochim. Biophys. Acta.* 1023: 25–33.

Tepper, A. D., P. Ruurs, T. Wiedmer, P. J. Sims, J. Borst, and W. J. van Blitterswijk. 2000. Sphingomyelin hydrolysis to ceramide during the

execution phase of apoptosis results from phospholipid scrambling and alters cell-surface morphology. *J. Cell. Biol.* 150:155–164.

Vanderlick, T. K., and H. Möhwald. 1990. Model selection and shape transitions of phospholipid monolayer domains. *J. Phys. Chem.* 94:890–894.

Virtanen, J. A., P. Somerharju, and P. K. J. Kinnunen. 1988. Prediction of patterns for the regular distribution of soluted guest molecules in liquid-crystalline phospholipid membranes. *J. Mol. Electron.* 4:233–236.

Virtanen, J. A., M. Ruonala, M. Vauhkonen, and P. Somerharju. 1995. Lateral organization of liquid-crystalline cholesterol-dimyristoylphos-

phatidylcholine bilayers. Evidence for domains with hexagonal and centered rectangular cholesterol superlattices. *Biochemistry.* 34:11568–11581.

Wakelam, M. J., T. R. Pettitt, P. Kaur, C. P. Briscoe, A. Stewart, A. Paul, A. Paterson, M. J. Cross, S. D. Gardner, and S. Currie. 1993. Phosphatidylcholine hydrolysis: a multiple messenger generating system. *Adv. Sec. Messeng. Phosphoprot. Res* 28:73–80.

Wang, M. M., M. Olsher, I. P. Sugàr, and P. L. G. Chong. 2004. Cholesterol superlattice modulates the activity of cholesterol oxidase in lipid membranes. *Biochemistry.* 43:2159–2166.